Precipitates on Dislocations

Literature study

S.M. Vonk

Delft University of Technology and TATA STEEL

Precipitates on Dislocations

Literature study

by

S.M. Vonk

A literature study submitted to the
Delft Institute of Applied Mathematics
at the faculty EEMCS of the TU Delft
in partial fulfilment of the requirements

for the degree

MASTER OF SCIENCE
in
APPLIED MATHEMATICS

in the specialisation of Computational Science and Engineering.

Delft, The Netherlands
March 2016

This thesis is confidential and cannot be made public.

The contents of this report are the exclusive property of Tata Steel Nederland Technology BV and are confidential. The contents of this document must not be disclosed to any third party without the prior written consent of Tata Steel Nederland Technology BV which, if given, is in any case conditional upon that party indemnifying Tata Steel Nederland Technology BV against all costs, expenses and damages which might arise as a result of the use of the contents. Care has been taken to ensure that the contents of this report are accurate, but Tata Steel Nederland Technology BV and affiliates do not accept responsibility for errors or for information that is found to be misleading. Suggestions for or descriptions of the use of products or the application of products or methods of working are for information purposes only, and Tata Steel Nederland Technology BV and affiliates accept no liability in respect thereof. Before using information or products supplied or manufactured by Tata Steel Nederland Technology BV or affiliates the user should make certain that they are suitable for their purpose. For further information or assistance, please contact Tata Steel Nederland Technology BV.

COPYRIGHT AND DESIGN RIGHT - © 2016 - TATA STEEL NEDERLAND TECHNOLOGY BV
COVER IMAGE: BLAST FURNACE 4 PORT TALBOT - TATA STEEL EUROPE LIMITED 2016 (IMAGE LIBRARY)

Precipitates on Dislocations

Literature study

by

S.M. Vonk

Abstract: Many models for the nucleating and growing precipitates have been developed. Each model with their own advantages and disadvantages. Only few of those models are made for heterogeneous nucleation (on dislocations). In this literature study, one of these models (by Zurob et al. (2002)) is explained, analysed and tested for different values of the model parameters and different initial values. This model exists of three different models: a precipitation, a recovery and a recrystallisation model, each interacting with the other ones. For one of this models: the precipitation model, the differential equations are derived, improvements are made and the final results are compared to the results obtained by Tata Steel (Kranendonk (2005)). The derived differential equations are solved using a different numerical methods: the Backward Euler method, the Backward Euler method combined with Forward Euler and a build-in MATLAB function Ode15s. The model shows to be flexible, but still has some drawbacks. A new model will be developed during the continuation of the Master thesis. One should think of a multi-component model for a combination of different types of precipitates together with a distribution model for the precipitate radius.

Keywords: Model by Zurob et al., precipitation, dislocations, nucleation, growth, $NbCN$ precipitate, backward euler, forward euler, 0de15s.

Student number:	4085299	
Project duration:	December 7, 2015 - September 10, 2016	
Daily supervisors:	Dr. ir. D. den Ouden,	TU Delft
	Dr. W. Kranendonk,	Tata Steel Europe IJmuiden
Overal supervisor:	Dr. ir. F.J. Vermolen ,	TU Delft
Responsible professor	Prof.dr.ir. C. Vuik,	TU Delft

Preface

This document is the result of my literature study carried out at the University of Technology at Delft, The Netherlands in cooperation with Tata Steel at IJmuiden, The Netherlands. This literature study is part of my Master Thesis at the chair of Numerical Analysis, in partial fulfilment of the requirements for the degree Master of Science in Applied Mathematics.
I wish to thank all people involved in this project, with a special thanks to Fred Vermolen, Dennis den Ouden and Winfried Kranendonk for proposing and supervising this project.

S.M. Vonk
March 29, 2016

Contents

List of Figures vii

List of Tables ix

List of Algorithms xi

1 Introduction 1

2 Preliminaries in metallurgy 3
- 2.1 Crystal Structure 3
- 2.2 Thermodynamics and Phase Diagrams 3
- 2.3 Diffusion 5
- 2.4 Precipitation 6
- 2.5 Dislocations 7
- 2.6 Metalworking Techniques 9

3 Mathematical Model 11
- 3.1 Recrystallisation, recovery and precipitation model by Zurob et al. 12
  - 3.1.1 Stage 1: Nucleation and growth 12
  - 3.1.2 Stage 2: Growth and coarsening 15
- 3.2 Implementation 16

4 Numerical methods 17
- 4.1 Integration methods 17
  - 4.1.1 Backward Euler 18
  - 4.1.2 Backward Euler combined with Forward Euler 18
  - 4.1.3 MATLAB Ode15s 20
- 4.2 Non-linear equations 20

5 Computational issues 23
- 5.1 Interface concentrations 23
- 5.2 Coarsening function 24
- 5.3 Unstable solutions 25

6 Numerical Results 27
- 6.1 Integration methods 27
- 6.2 Coarsening function 30
- 6.3 Variable variation 31
  - 6.3.1 Initial precipitate number density and mean radius 32
  - 6.3.2 Temperature 33
  - 6.3.3 Dislocation density 39
  - 6.3.4 Chemical composition 40

7 Concluding remarks and future work 43

A The recrystallization model and recovery model as developed by Zurob et al. 45

B Dimensional analysis of the differential equation for the precipitate number density N in the Zurob model 47

C Conversion formulas as used in the simulations 49

D Standard settings as used in the simulation 51

Bibliography 53

Nomenclature **55**

List of Figures

2.1 A part of a metal with a body-centred cubic (bcc) crystal structure (left) and a face-centred cubic (fcc) crystal structure (right). Image from Wikipedia (2016c). . . . 3
2.2 Illustration of a spontaneous change in the state of a system and the associated states. Image from Learning Geology (2015). . . . 4
2.3 Phase diagram of iron-carbon (steel). Image from Nair (2015). . . . 5
2.4 Different types of diffusion. Images from Cdan (2015). . . . 6
2.5 Defects in the crystal structure. . . . 7
2.6 Illustration of the movement of an edge dislocation. Image from Academic Resource Center (2015). . . . 8
2.7 Illustration of the Burgers vector for both type of dislocations. Image from Wikipedia (2016b). . . 8
2.8 Principle of a LD (Linz-Donawitz) converter. Image from Wikipedia (2016e). . . . 9
2.9 Illustration of the hot rolling and the processes that take place during this process. Image from Rendy Yusman (2011). . . . 10

3.1 An illustration of the connection between the three processes of our interest, with the dislocations as driving force of these processes. . . . 11
3.2 Schematic representation of the energy changes ΔG. Image from Perez et al. (2008). . . . 14
3.3 Coarsening function by Deschamps and Brechet (1999). . . . 15

4.1 Stability regions of various numerical integration methods in the complex plane. . . . 18
4.2 Stability regions (exterior of the curves) for the 1-5th BDF methods in the complex plane. . . . 20
4.3 Zoomed in stability region (exterior of the curves) for the 1-5th BDF methods in the complex plane. . . . 20

5.1 Plot of the coarsening function F_c against R/R^*. . . . 24
5.2 Illustration of the time steps at the end of the time interval. . . . 25

6.1 Simulation results with standard settings 28
6.2 Precipitate mean diameter using MATLABs Ode15s method and axes from the other methods. . 29
6.3 Volume fraction in time using the Backward Euler with Forward Euler method. . . . 29
6.4 Simulation results using BE compared to simulation by Tata Steel using Runge-Kutta 4. . . . 29
6.5 Coarsening function by Perrard et al. (2007). . . . 30
6.6 Coarsening function by Perez et al. (2008). . . . 30
6.7 Saturation based coarsening function. . . . 30
6.8 Saturation in time. . . . 30
6.9 Coarsening functions in time (using Euler Backward with Picard in the implementation). . . . 31
6.10 Simulation results for different initial values at 850 °C and $\rho = 3.27 \times 10^{14}$ m^{-2}. . . . 32
6.11 Volume fraction against temperature for alloy N1. . . . 33
6.12 Illustration of the construction of a PTT curve. . . . 34
6.13 Volume fraction in time for different temperatures with $\rho = 3.27 \times 10^{14}$ m^{-2}. . . . 34
6.14 The precipitate-time-temperature curve with $\rho = 3.27 \times 10^{14}$ m^{-2}. . . . 35
6.15 Precipitate-time-temperature curve on a logarithmic time scale and various temperature cooling curves. . . . 35
6.16 Simulation results for different temperatures and $\rho = 3.27 \times 10^{14}$ m^{-2}. . . . 36
6.17 Linear (setting (a)) and non-linear (setting (b)) temperature curves in time. . . . 36
6.18 Simulation results for a linear temperature increase and $\rho = 3.27 \times 10^{14}$ m^{-2}. . . . 37
6.19 Volume fraction and equilibrium volume fraction corrected for the Gibbs-Thomson effect in time. . . . 37
6.20 Simulation results for a non-linear temperature increase and $\rho = 3.27 \times 10^{14}$ m^{-2}. . . . 38

6.21 Volume fraction and equilibrium volume fraction corrected for the Gibbs-Thomson effect in time. 38
6.22 Simulation results for different dislocation densities at 850 °C. 39
6.23 Simulation results for different chemical compositions at 850 °C and $\rho = 3.27 \times 10^{14}$. 41

List of Tables

6.1 Precipitation parameters used in the simulations. 27
6.2 Numerical parameters used in the simulations. 27
6.3 Alloy composition of alloy N1 used in the simulations. 27
6.4 Overview of the different integration methods by time, number of iterations and error. 28
6.5 Differences in implementation between this literature study and Tata Steel 29
6.6 Various initial values chosen in the simulations. 32
6.7 Solvus temperatures for the different alloys described in Table 6.8. 33
6.8 Alloy composition of alloys N1, N2 and N4 used in the simulations. 40
6.9 Initial weight percentages and fractions of the precipitate elements together with the solvus temperatures. 40

C.1 Used symbols in the conversion formulas 49

List of Algorithms

4.1 Euler Backward with adaptive time step algorithm 19
4.2 Euler Backward and Forward Euler with adaptive time step algorithm 19
5.1 Adjusted algorithm (general version) with a different step size selection 26

1

Introduction

Precipitates play a very important role in the process of steel making and the final product steel. They can increase the strength of steal and decrease the growth of grains. Precipitation strengthening and small ferrite grains form the basis for the strength in High-Strength Low-Alloy (HSLA) steel, also named microalloying steels. This product group finds wide application in automotive, construction and energy (pipelines). The main alloying elements for precipitates in HSLA are niobium, titanium and vanadium. Moreover, precipitation strengthening is also increasingly being used as an additional strengthening mechanism in Advanced High Strength Steels (AHSS). Controlling and optimization of precipitation for both the hot rolling process as well as the annealing process is, therefore, essential.

Experiments on precipitation kinetics are time consuming, laborous and demand very special equipment. Models which describe the precipitation kinetics are therefore an essential addition to the experimental tools. Such models should (and can) reduce the development time for new steel grades, support the solution of production problems, support the optimisation of processes and improve the design of experimental tests. It would be therefore profitable to develop and improve new and existing models for (niobium) precipitation in steel.

These precipitates can grow at different spots in the steel: on grains, at grain boundaries, at dislocations, etc. The nucleation of precipitates on grains is called homogeneous nucleation, and the nucleation of precipitates on dislocations and other defects in the steel is called heterogeneous nucleation. Several models for both types of nucleation have been developed, but most of them just return the mean diameter and the density of the precipitates, whereas some would like to have a distribution for the diameter of the precipitates.

Den Ouden (2015) constructed a model with distributions for the diameter of the precipitates, but primarily for homogeneous nucleation. Since, heterogeneous nucleation seems to play a key role during plastic deformation of steel, which occurs for example during the hot rolling process, the goal of this Master Thesis is to make a new model with distributions for the diameter of the precipitates, but now for heterogeneous nucleation and with a multi-component part. Multi-component meaning that, contrary to some models, multiple types of precipitates (Nb(C,N), AlN, MnS, etc.) can be involved and analysed at the same time.

To understand the process of nucleating and growing precipitates on dislocations, a model by Zurob et al. (2002) is implemented and analysed. This model is limited to the mean diameter and density of the precipitates and describes only niobiumcarbonitride precipitates, but gives a good indication of how the precipitates nucleate and grow and also describes the interaction with recovery and recrystallisation (of dislocations). In this literature study we show the advantages and disadvantages of the model, give some improvements and end with a suggestion for future work during the Master Thesis.

The structure of this literature study is as follows. First in Chapter 2 some preliminaries of metallurgy are introduced, like some information on thermodynamics, phase diagrams and Gibb's free energy, but also information on dislocations and metalworking techniques is given to fully understand the process of steel making and the processes where precipitation plays a big role. After that in Chapter 3 the mathematical model by

Zurob et al. (2002) is derived and improved. Then in Chapter 4, various numerical methods are introduced to solve the obtained differential equations, which led to some computation issues which are then described and solved in Chapter 5. Finally in Chapter 6 the results of the simulations are shown, compared to experimental data and different initial values are chosen to see the effect on the solutions. And to finish off, some concluding remarks are made in Chapter 7, together with ideas for future work.

2

Preliminaries in metallurgy

To model the nucleating and growing of precipitates on dislocations, one needs some preliminaries in metallurgy. This chapter starts with an introduction to the crystal structure of metals. Thereafter a discussion is presented on thermodynamics and the phase diagram of steel. Then the diffusional concepts related to alloys are explained, followed by a short explanation of precipitation reactions due to this diffusion. These precipitation reactions can take place in two different ways: homogeneous and heterogeneous, which will be explained and linked to dislocations. Finally the process of steel making is presented and it is shown where the precipitation reactions we focus on occur during this process. The information presented in this chapter mostly originates from Porter and Easterling (1981) (especially Chapters 1, 2 and 5). Also some of the information originates from Den Ouden (2015) and the more detailed information about dislocations comes from Hull and Bacon (2001).

2.1. Crystal Structure

Metals can have different crystal structures, of which the body-centred and face-centred cubic crystal structure are the most common.

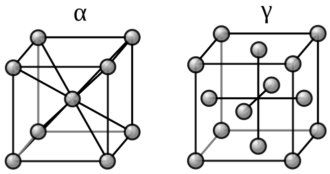

Figure 2.1: A part of a metal with a body-centred cubic (bcc) crystal structure (left) and a face-centred cubic (fcc) crystal structure (right). Image from Wikipedia (2016c).

When a metal solidifies from the liquid state, such crystals start to grow in the metal. The longer the metal takes to cool the larger the crystals grow in the metal. These crystals form the grains in the solid metal. Each grain is a distinct crystal with its own orientation. The areas between the grains are known as grain boundaries and are illustrated in Figure 2.5b (cross-section of the grains).

2.2. Thermodynamics and Phase Diagrams

To understand the concept of steel making and the process that takes place during the nucleating and growing of precipitates in steel, we first need to understand the thermodynamics of these processes. The keywords during this process are ‘free energy’ and ‘equilibrium’. However, for this we need four important definitions to start with:

Definition 2.1. *A **phase** is a region of space where the physical properties and composition are homogeneous and which is physically distinct from other parts of the system.*

Definition 2.2. *A **system** is an alloy that can exist as one phase or a mixture of phases.*

Definition 2.3. *A* ***component of the system*** *is one of the different elements or chemical compounds that make up the system.*

A system can have two types of properties:

1. Intensive properties, which are independent of size of the system (number of moles in the system), like the absolute temperature (T) and the pressure (P).
2. Extensive properties, which are directly proportional to the quantity of material in the system, like volume (V), internal energy (E), enthalpy (H), entropy (S) and free energy (G).

Definition 2.4. *A* ***phase transformation*** *is how one or more phases in an alloy (a system) changes into a new phase or mixture of phases.*

In phase transformations we are always concerned with changes towards equilibrium, where we mean equilibrium in the sense of the lowest free energy. For phase transformations that occur at constant temperature and pressure, the relative stability of a system is determined by its Gibbs free energy (G), measured in Joules (J), and defined by

$$G = H - TS,$$

where H is the enthalpy, T the absolute temperature in Kelvin (K) and S the entropy of the system. The enthalpy H is the sum of the internal energy E and the mechanical energy PV:

$$H = E + PV,$$

where E is the internal energy of the system in Joules (J), both kinetic and potential, P is the pressure in the system in Joules per cubic meter (J/m^3) and V is the volume of the system in cubic meters (m^3). It is good to notice, that in condensed phases like solid and liquid, the value of PV is much smaller than the internal energy E and the heat content of the system H is therefore close to this internal energy. When we plot the Gibbs free energy for a spontaneous change in the state of a system (with constant T and P), we get a graph like in Figure 2.2. The driving force behind a phase transformation is the difference between the Gibbs free energy in a certain (non-)equilibrium state of the system and the equilibrium state, where the state is in equilibrium when the free energy of the system is at minimum, i.e.:

$$dG = 0.$$

The intermediate states $dG \neq 0$ are unstable. From mathematics we know that when $dG = 0$, we have found a minimum or maximum, however we are only interested in the minimum free energy. Also, we can have a purely local minimum or a global minimum, which respectively corresponds to a metastable or a stable equilibrium. Given time, systems in a metastable state will transform to a stable state. However, the system then first has to overcome the energy maximum between the metastable and stable state, which is called the activation energy (Figure 2.2: E_a) and will determine the rate of the transformation.

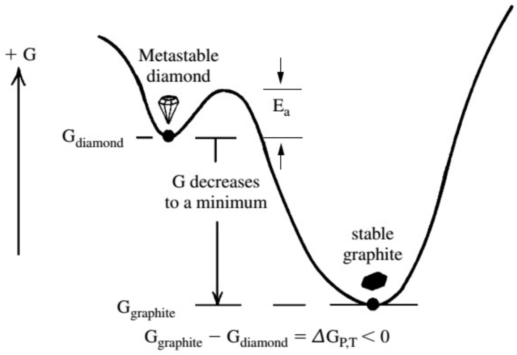

Figure 2.2: Illustration of a spontaneous change in the state of a system and the associated states. Image from Learning Geology (2015).

Using the Gibbs free energy plots for different temperatures, a phase diagram for alloys can be constructed. This derivation will not be given in this literature study, but an example can be found in Porter and Easterling (1981).

Since the focus of this thesis will be on steel, the phase diagram for iron-carbon is given in Figure 2.3. In this figure different phases of the system are shown for different temperatures (vertical axis) and different weight percentages of carbon (horizontal)[1]. Examples of these phases are Austenite and Ferrite, which also correspond to a crystal structure as described in Section 2.1 (Austenite $\leftrightarrow \gamma \leftrightarrow$ fcc, Ferrite $\leftrightarrow \alpha \leftrightarrow$ bcc). However, the probability that one has a system that is in such an equilibrium state is small. For a system to reach such a state or for us to model it, we need to introduce the concept of diffusion. Some of these phase transformations are not diffusion driven, but during this thesis we will only focus on diffusional phase transformations.

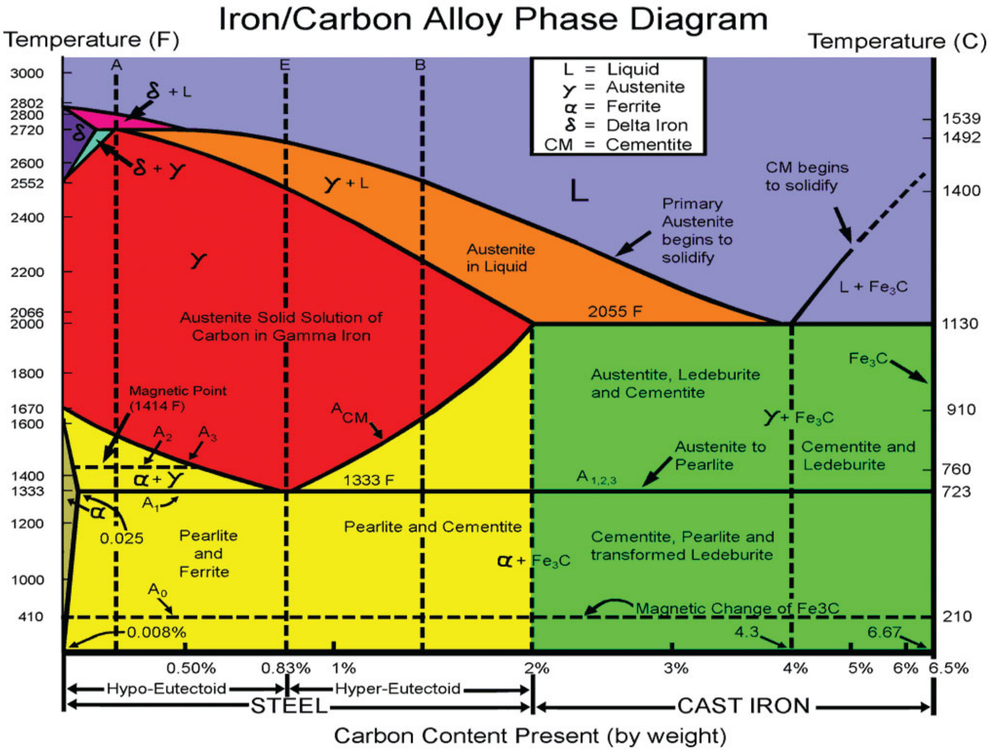

Figure 2.3: Phase diagram of iron-carbon (steel). Image from Nair (2015).

2.3. Diffusion

The concept of diffusion is based on the principle of the system wanting to reach the state with the lowest Gibbs free energy. Diffusion is basically the random movement of atoms. There can be distinguished two types of diffusion: interstitial and substitutional diffusion. For this we need to understand the concept of interstitial and substitutional atoms. Interstitial atoms are significantly smaller than the atoms of the solvent, and can thereby move between the other atoms freely. Substitutional atoms are larger or of approximate equal size as the solute atoms and can thereby not move between the other atoms, but need vacancies to move around. Both types of atoms are shown in Figure 2.5b. Since the interstitial atoms are smaller, they are forced their way between the solvent atoms, as shown in Figure 2.4a. This is called interstitial diffusion. The movement of substitutional atoms is called substitutional diffusion and is illustrated in Figure 2.4b. Here a solute atom will move to a vacant place in the solvent matrix. Since substitutional diffusion needs vacancies which only appear in small numbers, whereas interstitial diffusion occurs without vacancies, in general substitutional diffusion rates are much lower than interstitial diffusion rates.
For both types of diffusion we can assume that Fick's second law can be used to model how diffusion causes

---

[1] Some phase diagrams use a weight or molar fraction to measure the composition of the system.

the concentration to change with time:

$$\frac{\partial C_B}{\partial t} = \frac{\partial}{\partial x}(D_B \frac{\partial C_B}{\partial x}),$$

where C_B is the concentration of the solute atoms and D_B the diffusion constant of the solute atoms. When the diffusion constant has no variations with concentration of space, we find

$$\frac{\partial C_B}{\partial t} = D_B \frac{\partial^2 C_B}{\partial x^2}.$$

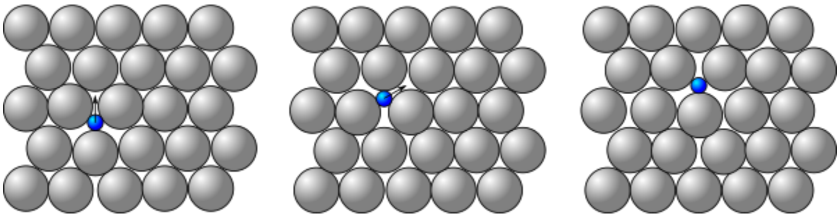

(a) Illustration of interstitial diffusion.

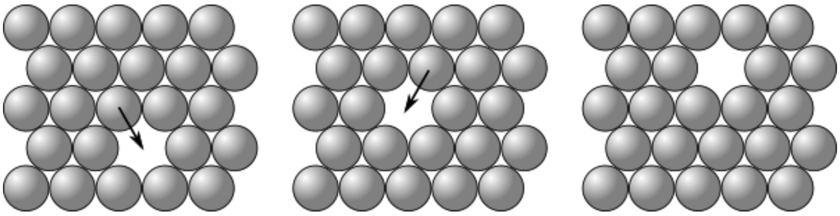

(b) Illustration of substitutional diffusion.

Figure 2.4: Different types of diffusion. Images from Cdan (2015).

2.4. Precipitation

In multi-component systems, like steel, many different phases can occur, which depend on the temperature. Five types of phase transformations can occur between different phases, of which almost all take place by diffusional nucleation and growth. However, we are primarily interested in the phase transformation due to precipitation reactions, which can be described by

$$\alpha \rightarrow \alpha^* + \beta,$$

where α is the phase before the transformation, and α^* and β are the phases after the transformation. When starting with a system in a supersaturated metastable solid phase α and a precipitation reaction occurs, the resulting system will consist of the α^* and β phases. Here α^* is a solid phase with lower Gibbs energy than α but with the same crystal structure and β is a (meta)stable precipitate phase. Looking back at the phase diagram in Figure 2.3, an example of this could be the phase transformation from austenite to austenite with ferrite ($\gamma \rightarrow \gamma + \alpha$).

There are three important concepts for precipitation:

1. Nucleation: the arise of precipitates from a supersaturated matrix.
2. Growth: the growing of precipitates. During this process the precipitates take atoms from the matrix to grow until equilibrium between the precipitates and the matrix has been reached.
3. Coarsening: the growth of large precipitates at the cost of small precipitates, also known as Ostwald ripening. The driving force for coarsening is the reduction of the interfacial energy and thereby the total free energy. By the growth of large precipitates and the disappearance of small ones the total interfacial area is reduced and, thus, the free energy. This mostly happens if the concentrations (of the precipitates compounds) in the matrix is near the equilibrium concentration.

All of these concepts can take place at the same time, so for the final model we also need the interaction between these three concepts.

2.5. Dislocations

The precipitation reaction as described before takes place by diffusional nucleation and growth. Two types of nucleation can take place: homogeneous and heterogeneous (on defects). The different types of heterogeneous nucleation have lower activation energies than homogeneous nucleation, and, therefore, heterogeneous nucleation is the main mechanism in solids and liquids. In the thesis of Den Ouden (2015) the focus is mostly on homogeneous nucleation, and so the focus during this thesis will be mostly on heterogeneous nucleation.

As described in Section 2.1, metal alloys have a crystal structure, however, all real crystals contain some sort of imperfections which can have different shapes: point, line, surface or volume defects. These defects locally disturb the arrangement of the atoms in the crystal structure and in this way have an important effect on the properties of the metal alloys. These defects are the locations for heterogeneous nucleation. Some of the defects like vacancies, dislocations, stacking faults and grain boundaries are shown in Figure 2.5b. In this thesis, the main focus will be on the nucleation and growth of precipitates on dislocations.

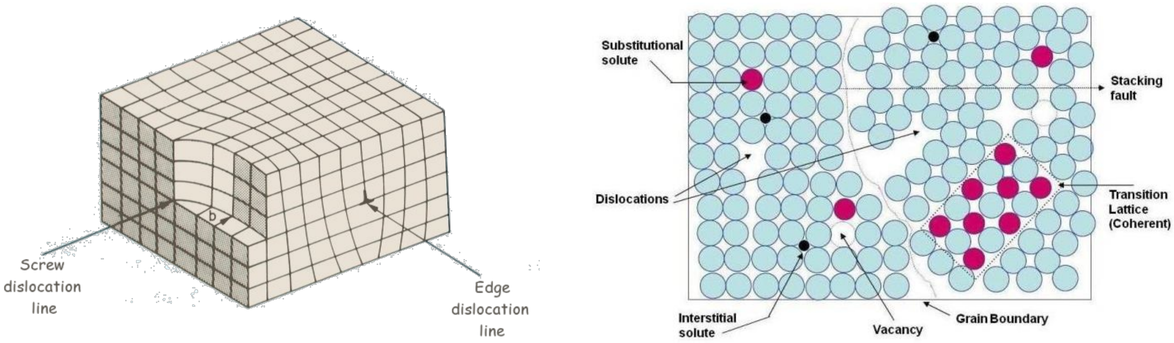

(a) Combination of two types of dislocations. Image from Rey (2015).

(b) Crystal structure with several different defects. Image from Shah (2012).

Figure 2.5: Defects in the crystal structure.

All these defects increase the free energy of the material, which is an unwanted effect. Each defect has his own type of free energy contribution, for example a dislocation is associated with an increased elastic energy and a grain boundary with an increased interface energy. The combination of a precipitate and the defect results in a lower free energy (for a dislocation a lower elastic energy) and thereby reducing the total free energy of the material. The equation for the energy change due to a heterogeneous reaction therefore becomes

$$\Delta G_{het} = V(\Delta g_v - \Delta g_s) + A\gamma + \Delta G_d, \tag{2.1}$$

where Δg_v is the general free energy reduction, Δg_s is the misfit strain energy[1], $A\gamma$ the increase of free energy due to interfacial energy [2] and ΔG_d the free energy release due to the reduction of the elastic energy associated with dislocations. The sign of Δg_v is dependent on the saturation of the matrix. It has a negative sign for an over-saturated matrix and a positive sign for an under-saturated matrix. Also, we will assume in this thesis, that we deal with incoherent particles and the misfit strain energy can be approximated by zero.

To fully understand the energy changes due to heterogeneous nucleation, we need more information about dislocations and their geometry. Starting with the types of dislocations there exists, Figure 2.5a shows both of them.

1. An edge dislocation, *and*
2. a screw dislocation.

The edge dislocation can be simulated as follows: let a surface of the crystal structure be broken, such that that the faces of the crystal are separated. Now an additional half-plane of atoms can be inserted in this

---

[1] In general the transformed volume will not perfectly fit into the original space occupied by the matrix, which will result in this free energy increase.

[2] The creation of a nucleus with area A will give a free energy increase of $A\gamma$, assuming that the α-β interfacial energy is isotropic.

opening, which results in an edge dislocation. Both positive and negative edge dislocations can exist, respectively meaning an additional half-plane from above the broken surface, illustrated with a ‘$\perp'$ or an additional half-plane from below the broken surface, illustrated with a ‘$\top'$. It is good to point out, that after an edge dislocation has formed, edge dislocations can move to the side of the crystal under a shearing deformation of the crystal, as shown in Figure 2.6.

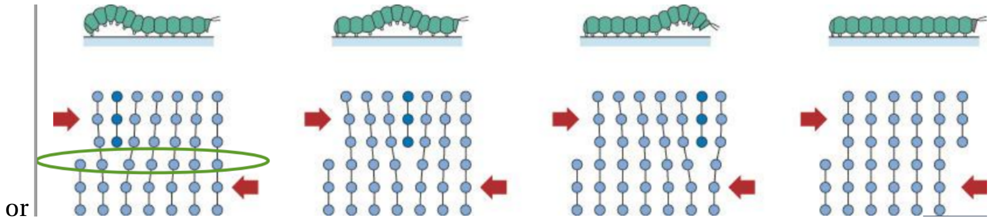

Figure 2.6: Illustration of the movement of an edge dislocation.
Image from Academic Resource Center (2015).

The screw dislocation can be seen as a simple displacement of part of the crystal structure, relative to the other part of the crystal structure. In Figure 2.5a both dislocations are shown and the difference between the edge and the screw dislocation becomes clear. As with edge dislocations, two directions of the dislocation can be distinguished. Contrary to the edge dislocations, however, screw dislocation are distinguished between left-handed and right-handed, meaning the direction of the dislocation when looking down the dislocation line. When a clockwise circuit is made round it, it is referred to as a right-handed screw dislocation and when a counter-clockwise circuit is made round it, it is referred to as a left-handed screw dislocation. Mixtures of both edge and screw dislocations also exist, as shown in Figure 2.5a. To formally describe the dislocation, we introduce the definition of the *Burgers circuit*.

Definition 2.5. *The **Burgers circuit** is any atom-to-atom path, a closed loop, containing the dislocations in the crystal structure (Figure 2.7).*

Another important concept is that of the *Burgers vector*, which together with the Burgers circuit defines the dislocation. The Burgers vector's magnitude and direction is best understood when the dislocation-bearing crystal structure is first visualised without the dislocation, that is, the perfect crystal structure. For this we use Figure 2.7 as an illustration. In this perfect crystal structure, a rectangle is drawn surrounding the site of the original dislocation's origin. The lengths and widths of this rectangle are integer multiples of the unit-cell-edge length. Once the surrounding rectangle (*MNOP*) is drawn, the dislocation can be introduced. This dislocation will have the effect of deforming, not only the perfect crystal structure, but the rectangle as well. The *MNOP*-rectangle could have one of its sides disjointed from the perpendicular side, severing the connection of the length and width line segments of the rectangle at one of the rectangle's corners, and displacing each line segment from each other. What was once a rectangle before the dislocation was introduced, is now an open geometric figure whose opening defines the direction and magnitude of the Burgers vector.

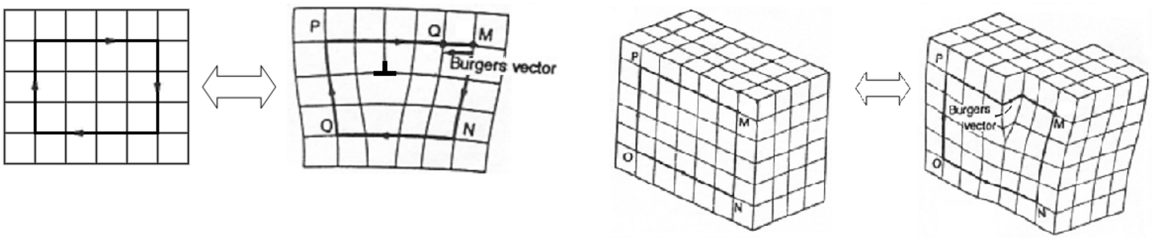

Figure 2.7: Illustration of the Burgers vector for both type of dislocations. Image from Wikipedia (2016b).

The Burgers vector is closely related to the dislocation density, a parameter of interest, since it influence both the nucleation and growth of precipitates.

2.6. Metalworking Techniques

In the process of steel making, a series of metalworking techniques is used wherein precipitation reactions play a role. The process will be explained in general and the parts which include these precipitation reactions will be explained more thoroughly.

1. Reduction of iron oxides (ore) to iron metal

    - Installation/process: blast furnace (around 2000 °C),
    - Metallurgical processes: reduction reactions.

    The process of steel making starts with iron ore. This is a chemical composition consisting of iron oxides (Fe_xO_y). At high temperatures the carbon level in these oxides is reduced, resulting in pig iron (liquid iron, containing around 4.4 wt% carbon) and CO_2.

2. Lowering of carbon concentration and adding alloying elements

    - Installation/process: basic oxygen steel plant (1550 °C),
    - Metallurgical processes: oxidation, dissolution (of alloying elements).

    The pig iron is transported to a steel mill, at which the carbon level in the iron is reduced. When the pig iron arrives at the steel mill it is carbon-rich (around 4.8 wt-%), but for the pig iron to be called steel, it has to be carbon-low (less than 2 wt-% carbon). To reduce the carbon in the mixture, we use the following reaction

    $$C + O_2 \rightarrow CO_2.$$

    In Figure 2.8 the process of blowing oxygen into the pig iron to get the reaction, is illustrated. During this process also several alloying elements like Ti (Titanium), Nb (Niobium) or V (Vanadium) are added, to change the mechanical properties of the resulting steel. This is an important part to point out, since especially these allloying elements are the ones that will form precipitates later on in the process. The result of the so called *Basic oxygen steelmaking* (Wikipedia (2015)) can be then poured into big molds of around 230 mm thick and 10-20 ton. The structure of the resulting strips has large grains and can contain already precipitates.

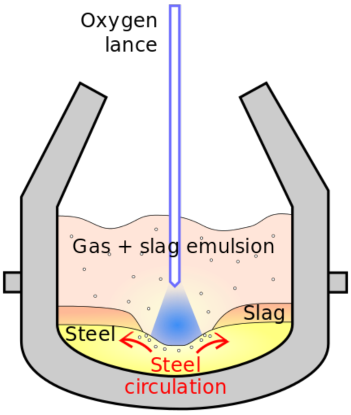

Figure 2.8: Principle of a LD (Linz-Donawitz) converter. Image from Wikipedia (2016e).

3. Rolling of strip from 230 mm to 2-25 mm

    - Installation/process: hot strip mill (1250-850 °C),
    - Metallurgical processes: deformation, recrystallisation, recovery, **precipitation**, transformation (oxidation).

The thick slabs will then arrive at the hot strip mill, where the slabs are rolled in a roughing and finishing mill to the final thickness between 2 and 25 mm. The deforming of the steel is an application of elastic and/or inelastic deformation and can therefore be described with a stress-strain relation.

Between the rolls, recrystallisation and recovery can take place. Recrystallisation is the process of reducing dislocations (created by plastic deformation) by nucleation and growing of new, dislocation free, grains whereas recovery is reducing the dislocation density by annihilation and redistribution. An illustration of part of this process is shown in Figure 2.9. The last process of hot rolling: transformation, is the process where the steel transforms from the austenite to the ferrite phase, and takes place at the end of the hot strip rolling, when the strip is cooled down to around 600-700 °C.

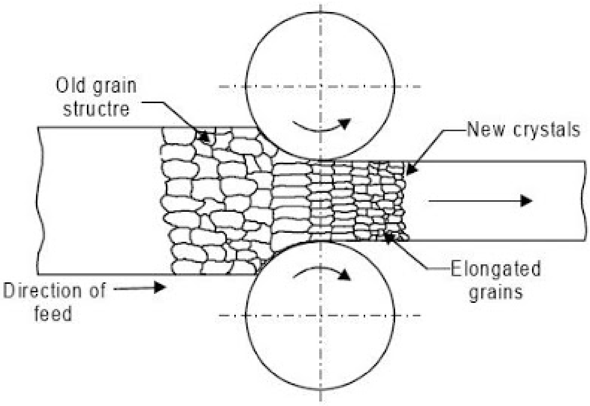

Figure 2.9: Illustration of the hot rolling and the processes that take place during this process. Image from Rendy Yusman (2011).

4. Rolling of strip from 2-5 mm to 0.2-1.5 mm (optional)
    - Installation/process: cold strip mill and annealing line (20-150 °C),
    - Metallurgical processes: deformation (cold strip mill), recrystallisation, recovery, **precipitation**, transformation (annealing line).

The goal of this part of the process is to control the shape, size and thickness of the steel. The thickness is reduced by cold rolling, which results in a hard and difficultly deformable strip. To recover the formability again, the rolled strip is annealed (600-750°C) where recovery, recrystallisation, precipitation and, depending on the temperature, transformation will take place. Contrary to the metallurgical process that took place at the hot strip mill, this process mainly takes place in the ferrite phase instead of the austenite phase.

5. Coating and painting (optional)
    - Installation: coating and painting line,
    - Metallurgical processes: tempering (coating), hydrogen embrittlement(coating).

This part of the steel making process only concerns the corrosion protection and/or outlook of the strip and is not relevant for the subject of this thesis.

3

Mathematical Model

During softening after deformation at high temperatures or during annealing after cold rolling, three processes are of our main interest: precipitation, recrystallisation and recovery. Each of these processes strengthens or weakens the other processes. The different connections in Figure 3.1 will now be explained (based on Zurob et al. (2002)):

- Green line: When precipitates are present they slow down the process of recrystallisation and in return a decrease in the dislocation density due to recrystallisation reduces the number of precipitates nucleation sites available and therefore the rate of precipitation.

- Pink line: The driving force for both recovery and recrystallisation is the stored energy of deformation (dislocations), meaning that the process of recovery will reduce this driving force available in the material for the migration of the recrystallisation boundaries. Therefore the recovery and recrystallisation process are competing processes.

- Blue line: When precipitates are present at dislocations they slow down the process of recovery and in return recovery can delay the progress of precipitation by reducing the number of available nucleation sites.

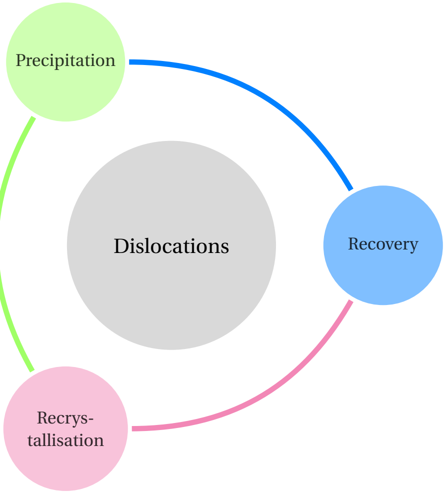

Figure 3.1: An illustration of the connection between the three processes of our interest, with the dislocations as driving force of these processes.

It is clear that these three processes are linked and therefore they cannot be viewed separately to state conclusions on the nucleating and growing of precipitates on dislocations.

3.1. Recrystallisation, recovery and precipitation model by Zurob et al.

Zurob et al. (2002) introduced a combination of the three models (a recrystallisation, a recovery and a precipitation model) to describe the growth and nucleation of precipitates on dislocations. In this combination each model interacts with the other models as described in the introduction. The model by Zurob et al. (2002) primarily describes the nucleation, growth and coarsening of the precipitates and not the dissolving.

Since the the focus in this thesis is on the modelling of the nucleation and growth of precipitates, we will first model the precipitation part of the Zurob model before we will link this to the recovery and recrystallisation models (found in Appendix A). The model for precipitation is described using two stages. The first stage describes the part when precipitates are nucleating and growing, whereas the second stage describes the part when precipitates are growing and coarsening will take place. The two stages and the switch between these two will be explained more thoroughly in the coming section, but will result in the following model for precipitation:

- Precipitation stage 1 (Nucleation and Growth)

$$\frac{dN}{dt} = (N_{total} - N)\left(\frac{D_{pipe}x^M_{Nb}}{a^2}\right)\exp\left(\frac{-\Delta G^*}{k_b T}\right),$$

$$\frac{dR}{dt} = \frac{D_{eff}}{R}\frac{C^M_{Nb} - C^{Eq}_{Nb}\exp(R_0/R)}{C^P_{Nb} - C^{Eq}_{Nb}\exp(R_0/R)} + \frac{1}{N}\frac{dN}{dt}(\alpha_n R^* - R).$$

- Precipitation stage 2 (Growth and Coarsening)

$$\frac{dN}{dt} = F_c\left(\frac{4}{27}\frac{C^{Eq}_{Nb}}{C^P_{Nb} - C^{Eq}_{Nb}}\frac{R_0 D}{R^3}\right)\left(\frac{R_0 C^M_{Nb}}{R(C^P_{Nb} - C^M_{Nb})}\left(\frac{3}{4\pi R^3} - N\right) - 3N\right),$$

$$\frac{dR}{dt} = (1 - F_c)\left.\frac{dR}{dt}\right|_{\text{growth}} + F_c\left.\frac{dR}{dt}\right|_{\text{coarse}}.$$

Symbols that are not explained in the text, can be found in the nomenclature.

3.1.1. Stage 1: Nucleation and growth

Focusing on the nucleation of precipitates first, we assume it occurs on dislocations exclusively. The rate of nucleation is given by

$$\frac{dN}{dt} = \left(1 - \frac{N}{N_{total}}\right)N_{total}Z\beta^*\exp\left(\frac{-\Delta G^*}{k_b T}\right),$$

where N_{total} is the number of nucleation sites that is available, Z is the Zeldovich non-equilibrium factor, β^* is the rate of atomic attachment to the critical nucleus, ΔG^* is the energy barrier needed for the nucleation to take place, k_B is the Boltzman constant and T is the temperature given in K. N_{total} is defined as

$$N_{total} = \frac{F\rho}{b}, \tag{3.1}$$

where b is the length of the Burgers vector, F a fitting parameter and ρ the dislocation density. Furthermore, we assume that the precipitates are spherical, leading to the approximation of $Z\beta^*$

$$Z\beta^* \approx \frac{D_{pipe}x^M_{Nb}}{a^2}.$$

Zurob et al. (2002) used the concentration of niobium in the matrix C^M_{Nb} in this approximation, but after dimensional analysis (Appendix B), we find this should be the above stated x^M_{Nb}, which is a molar fraction. This leads to the following equation, as the describing equation for the nucleation rate during the first stage.

$$\left.\frac{dN}{dt}\right|_{nucleation} = (N_{total} - N)\left(\frac{D_{pipe}x^M_{Nb}}{a^2}\right)\exp\left(\frac{-\Delta G^*}{k_b T}\right) \tag{3.2}$$

The activation energy ΔG^* and the accessory critical radius R^* are estimated using the expression for the free energy of precipitate formation (Equation 2.1):

$$\Delta G = V\Delta g_v + A\gamma + \Delta G_d.$$

Zurob et al. (2002) define the free energy release due to the reduction of the elastic energy associated with dislocations by

$$\Delta G_d = -\frac{\mu b^2 R\ln(R/b)}{2\pi(1-\nu)} - \frac{\mu b^2 R}{5},$$

leading to the energy balance for heterogeneous nucleation:

$$\Delta G = V\Delta g_v + A\gamma - \frac{\mu b^2 R\ln(R/b)}{2\pi(1-\nu)} - \frac{\mu b^2 R}{5}, \tag{3.3}$$

where V and A are respectively the volume and the area of the precipitate, γ the interface energy, ν the Poisson ratio, μ the shear modulus and Δg_v the free energy change attending nucleation, also known as the chemical driving force. This chemical driving force is estimated by[1]

$$\Delta g_v = -\frac{k_B T}{v_{NbCN}} \ln\left(\frac{\text{matrix product}}{\text{solubility product}}\right) := -\frac{R_g T}{v_{m,NbCN}} \ln\left(\text{saturation}\right). \tag{3.4}$$

The saturation is the fraction of the matrix product and the solubility product. The matrix product is the product of the concentrations (in weight percentages) of the precipitate compounds in the matrix to the power of their stoichiometric ratio x (the ratio of carbon and nitrogen in the precipitate at equilibrium)

$$\text{matrix product} = wt\%Nb^M (wt\%C^M)^x (wt\%N^M)^{1-x},$$

and the solubility product is the product of the separate solubility products (Hudd et al. (1971))

$$\begin{aligned} K(NbCN) &= K(NbC)^x K(NbN)^{1-x} x^x (1-x)^{1-x}, \\ &= \left(\frac{wt\%Nb^{Eq}\, wt\%C^{Eq}}{x}\right)^x \left(\frac{wt\%Nb^{Eq}\, wt\%N^{Eq}}{1-x}\right)^{1-x} x^x (1-x)^{1-x}, \\ &= wt\%Nb^{Eq} (wt\%C^{Eq})^x (wt\%N^{Eq})^{1-x}. \end{aligned}$$

The saturation can be rewritten as

$$\text{saturation} = \frac{wt\%Nb^M}{wt\%Nb^{Eq}} \left(\frac{wt\%C^M}{wt\%C^{Eq}}\right)^x \left(\frac{wt\%N^M}{wt\%N^{Eq}}\right)^{1-x}, \tag{3.5}$$

and gives an indication of how close the matrix concentrations are to their equilibrium concentration. In isothermal conditions the system will move to a state of equilibrium and, thus, the saturation will approach one.

The equilibrium concentration in the matrix $wt\%Nb^{Eq}$ can be found by solving the following equation from Hudd et al. (1971).

$$\begin{aligned} &(wt\%Nb^{Eq})^4 (M_C M_N) + (wt\%Nb^{Eq})^3 (-2wt\%NbM_C M_N + wt\%CM_N M_{Nb} + wt\%NM_C M_{Nb}) \\ &+ (wt\%Nb^{Eq})^2 (-M_{Nb} M_N * K(NbC) - M_{Nb} M_C K(NbN) + (wt\%Nb)^2 M_C M_N - wt\%Cwt\%NbM_N M_N b \\ &- wt\%Nwt\%NbM_C M_{Nb}) + wt\%Nb^{Eq} (wt\%NbM_{Nb} M_N K(NbC) + K(NbN) wt\%NbM_C M_{Nb} \\ &- wt\%NK(NbC) M_{Nb}^2 - wt\%CK(NbN) M_{Nb}^2) + K(NbC) K(NbN) M_{Nb}^2 = 0, \end{aligned} \tag{3.6}$$

where the solubility products $K(NbN)$ and $K(NbC)$ are temperature dependent. The solvus temperature T_{sol}, the maximum temperature at which precipitates can form, is found by substituting $wt\%Nb^0$ in Equation (3.6) and solve for the temperature. During the isothermal and non-isothermal simulations in Chapter 6, the temperature should stay below this solvus temperature.

---

[1] The model works for several types of precipitates, but for this literature study we will focus on $NbCN$ precipitates only.

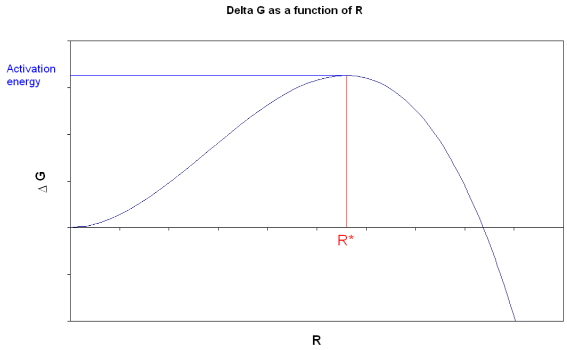

Figure 3.2: Schematic representation of the energy changes ΔG. Image from Perez et al. (2008).

Going back to the energy balance in Equation (3.3), a schematic representation of the energy changes of precipitate forming (Equation (3.3)) is given in Figure 3.2, where it can be seen that the activation energy ΔG^* is the maximum of ΔG. Therefore we take the derivative of ΔG to R, given in Equation (3.7) (note that Δg_v does not depend on R), and set it to zero to find the critical radius, where after we substitute the radius back into Equation (3.3) to find the activation energy.

$$\frac{d(\Delta G)}{dR} = 4\pi R^2 \Delta g_v + 8\pi R\gamma - \frac{\mu b^2}{2\pi(1-\nu)}(\ln(R/b)+1) - \frac{\mu b^2}{5} = 0 \tag{3.7}$$

Beside the rate of nucleation, we are also interested in the growth rate during the first stage. The growth rate of existing precipitates is given by

$$v = \frac{dR}{dt} = \frac{D_{eff}}{R}\frac{C^M - C^R}{C^P - C^R}, \tag{3.8}$$

where the concentrations C and effective diffusion coefficient refer to the elements in the precipitate (Nb, C, N). In the case of niobiumcarbonitrides Equation (3.8) can be formulated for each element in the precipitate, and all these formulations are equal. C^M is the concentration of the growth driving solute in the matrix, C^P the concentration of this solute in the precipitate and C^R the concentration of this solute in the matrix at the precipitate/matrix interface. The value of this precipitate/matrix interface concentration is modelled by the use of a Gibbs-Thomson equation (Zurob et al. (2002))

$$C^R = C^{Eq}\exp\left(\frac{R_0}{R}\right), \quad \text{where } R_0 = \frac{2\gamma v_{m,NbCN}}{R_g T}. \tag{3.9}$$

The effective diffusion coefficient D_{eff} is defined by

$$D_{eff} = D_{pipe}\pi b^2 \rho + D_{bulk}(1-\pi b^2\rho), \tag{3.10}$$

where the dislocation density ρ is taken constant for now and D_{pipe} and D_{bulk} are respectively the diffusion coefficients in the pipe and bulk.

The total growth rate of the precipitate mean radius during the first stage is the growth rate of the existing precipitates (Equation (3.8)) plus the contribution of the arrival of dN new nuclei in the existing population of precipitates. The contribution of the arrival of new nuclei is defined by

$$\frac{1}{N}\frac{dN}{dt}\left(\alpha_n R^* - R\right),$$

where α_n is a numerical factor, accounting for the fact that nucleated precipitates can grow only if their radius is slightly larger than the nucleation radius. This results in the full growth rate to be

$$\frac{dR}{dt} = \frac{D_{eff}}{R}\frac{C^M_{Nb} - C^{Eq}_{Nb}\exp(R_0/R)}{C^P_{Nb} - C^{Eq}_{Nb}\exp(R_0/R)} + \frac{1}{N}\frac{dN}{dt}(\alpha_n R^* - R). \tag{3.11}$$

3.1.2. Stage 2: Growth and coarsening

In the first stage of precipitation we considered simultaneously nucleation and growth (when the saturation (Equation (3.5)) is much larger than 1), whereas in the second stage of precipitation (when the saturation (Equation (3.5)) is near 1) we now consider a combination of growth and coarsening. During this second stage of precipitation the growth rate is slightly different from the one for the first stage, since it is a combination of the growth rate of pure growth and the growth rate of pure coarsening. When the mean radius of the precipitates is much larger than the critical radius, the equation for pure growth is valid, but when the mean radius is equal to the critical radius, the conditions for the standard LSW law are fulfilled (Deschamps and Brechet (1999)) and pure coarsening takes place[1]:

$$\left.\frac{dR}{dt}\right|_{\text{growth}} = \frac{D_{eff}}{R}\frac{C_{Nb}^{M} - C_{Nb}^{Eq}\exp(R_0/R)}{C_{Nb}^{P} - C_{Nb}^{Eq}\exp(R_0/R)}, \tag{3.12}$$

$$\left.\frac{dR}{dt}\right|_{\text{coarse}} = \frac{4}{27}\frac{C_{Nb}^{Eq}}{C_{Nb}^{P} - C_{Nb}^{Eq}}\frac{R_0 D}{R^2}. \tag{3.13}$$

A coarsening function F_c is used to combine the two growth rates to one equation for the growth rate of the second stage:

$$\frac{dR}{dt} = (1 - F_c)\left.\frac{dR}{dt}\right|_{\text{growth}} + F_c\left.\frac{dR}{dt}\right|_{\text{coarse}},$$

where we choose the coarsening function in accordance with Deschamps and Brechet (1999) to be

$$F_c = 1 - \operatorname{erf}\left(4\left(\frac{R}{R_0}\ln\left(\frac{C_{Nb}^{M}}{C_{Nb}^{Eq}}\right) - 1\right)\right). \tag{3.14}$$

Later on we will use the coarsening function to combine the differential equations for the precipitate number density N and the mean radius R of the first and second stage, resulting in a slightly different description for the growth rate.

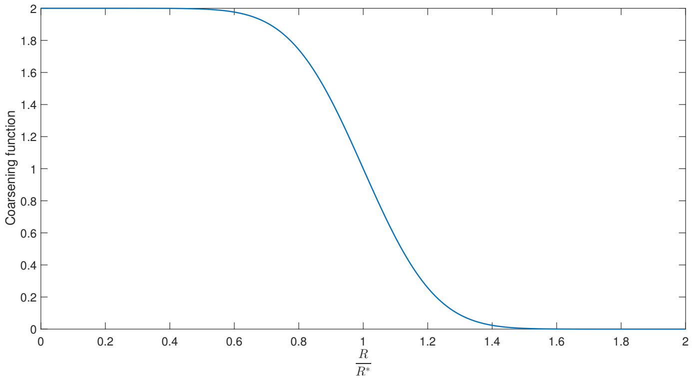

Figure 3.3: Coarsening function by Deschamps and Brechet (1999).

Other coarsening functions are defined by Perrard et al. (2007), Kranendonk (2005), and Perez et al. (2008), each with their own advantages and disadvantages.

Using the equation of the critical radius, the mean radius, and the mass balance, we find the following variation in the precipitate number density during coarsening in the second stage (using the derivation by Deschamps and Brechet (1999)):

$$\frac{dN}{dt} = \frac{4}{27}\frac{C_{Nb}^{Eq}}{C_{Nb}^{P} - C_{Nb}^{Eq}}\frac{R_0 D}{R^3}\left(\frac{R_0 C_{Nb}^{M}}{R(C_{Nb}^{P} - C_{Nb}^{M})}\left(\frac{3}{4\pi R^3} - N\right) - 3N\right). \tag{3.15}$$

---

[1] Several descriptions of the pure coarsening regime are developed, of which the one by Kreye (1970) takes into account the dislocations. It involves the fourth power of the mean radius ($1/R^4$), in contrast to the one used in this thesis, which involves the second power of the mean radius ($1/R^2$).

Multiplication of this variation by the coarsening function F_c is necessary to only take into account the effect of growth and coarsening when $F_c > 0$.

3.2. Implementation

As stated before, the precipitation model from Zurob et al. (2002) uses two stages which act successively:

- Precipitation stage 1 (Nucleation and Growth)

$$\frac{dN}{dt} = (N_{total} - N)\left(\frac{D_{pipe} x^M_{Nb}}{a^2}\right)\exp\left(\frac{-\Delta G^*}{k_b T}\right), \text{ where } N_{total} = \frac{F\rho}{b},$$
$$\frac{dR}{dt} = \frac{D_{eff}}{R}\frac{C^M_{Nb} - C^{Eq}_{Nb}\exp(R_0/R)}{C^P_{Nb} - C^{Eq}_{Nb}\exp(R_0/R)} + \frac{1}{N}\frac{dN}{dt}(\alpha_n R^* - R).$$

- Precipitation stage 2 (Growth and Coarsening)

$$\frac{dN}{dt} = F_c\left(\frac{4}{27}\frac{C^{Eq}_{Nb}}{C^P_{Nb} - C^{Eq}_{Nb}}\frac{R_0 D}{R^3}\right)\left(\frac{R_0 C^M_{Nb}}{R(C^P_{Nb} - C^M_{Nb})}\left(\frac{3}{4\pi R^3} - N\right) - 3N\right),$$
$$\frac{dR}{dt} = (1 - F_c)\left.\frac{dR}{dt}\right|_{\text{growth}} + F_c\left.\frac{dR}{dt}\right|_{\text{coarse}}.$$

The switch from stage 1 to stage 2 takes place at the moment when the following inequality from Deschamps and Brechet (1999) holds

$$-\left.\frac{dN}{dt}\right|_{\text{coarse}} > \left.\frac{dN}{dt}\right|_{\text{nucleation}}. \tag{3.16}$$

This is the moment when the decrease in precipitate density due to coarsening is larger than the increase of the precipitate density due to nucleation. Another option as provided by Kranendonk (2005) is to combine the two stages using the coarsening function F_c, which results in the following differential equations:

$$\frac{dN}{dt} = (1 - F_c)\left.\frac{dN}{dt}\right|_{\text{nucleation}} + F_c\left.\frac{dN}{dt}\right|_{\text{coarse}},$$
$$\frac{dR}{dt} = (1 - F_c)\left.\frac{dR}{dt}\right|_{\text{nucleation,growth}} + F_c\left.\frac{dR}{dt}\right|_{\text{coarse}},$$

where

- $\left.\frac{dN}{dt}\right|_{\text{nucleation}}$ equals Equation (3.2),
- $\left.\frac{dN}{dt}\right|_{\text{coarse}}$ equals Equation (3.15),
- $\left.\frac{dR}{dt}\right|_{\text{nucleation,growth}}$ equals Equation (3.11),
- $\left.\frac{dR}{dt}\right|_{\text{coarse}}$ equals Equation (3.12).

This combination of the two stages by the coarsening function has our preference, since it could occur when using the switch, that inequality (3.16) holds, but the coarsening function F_c returns 0, leading to a nucleation rate $\frac{dN}{dt}$ of 0, which is not the result we would physically expect.

Now that we have defined the differential equations, we can solve them to find N, the precipitate number density in time and R, the mean radius of precipitates in time. Since the differential equations are complex, they cannot be solved analytically, so we use multiple numerical time integration methods. These methods will be explained in the next chapter.

4

Numerical methods

In the implementation of the model, as described in Chapter 3, the differential equations have to be solved numerically. In this chapter different numerical integration methods for solving the differential equations will be described, evaluated and compared. Also various non-linear equation solvers needed, for example to solve Equation (3.7) for the activation energy, will be explained. More information on the basic mathematical concepts discussed in this chapter concerning numerical time integration methods, like stability regions, stiff equations and implicit and explicit methods can be found in Chapter 6 from *Numerieke Methoden voor Differentiaalvergelijkingen* by Vuik et al. (2015).

4.1. Integration methods

The differential equations obtained in Chapter 3 lead to an initial value problem (IVP) when adding initial conditions to the model. This IVP can be solved using various numerical integration methods, which can be divided into explicit and implicit methods. The difference between these two types of methods is that implicit methods require the solving of a (non-)linear equation in each time step, whereas explicit methods do not. It seems that the easy choice would be to use explicit methods, however, implicit methods have a larger stability region, meaning that a larger step size can be taken when using such a method. In Figure 4.1 the difference in stability regions between explicit methods (Forward Euler and Modified Euler) and implicit methods (Backward Euler) is clearly seen. A loose rule of thumb dictates that stiff differential equations require the use of implicit schemes because of their stability, whereas non-stiff problems can be solved more efficiently with explicit schemes (Wikipedia (2016d)). Because our IVP is indeed stiff [1] and we would like to be able to choose large step sizes, we choose an implicit method. Besides the character of the method, also the order or rate of convergence of the method is of importance. One could choose a higher order method to have a fast computation at the same accuracy. Unfortunately, also these higher order methods have the property of small stability regions. For example, in Figure 4.1 compare the stability regions of a first order method Backward Euler and a fourth order method Runge-Kutta 4. For our IVP we compare and analyse three numerical integration methods, each chosen because of their properties of having large stability regions. First we will use a simple Backward Euler method with adaptive time step, secondly a Backward Euler method combined with a Forward Euler method, also with adaptive time step and last a built-in MATLAB method: Ode15s. Moreover, we will discuss the adaptive time step control algorithm.

---

[1] This was found using the MATLAB Ode45 function.

(a) Forward Euler (interior of curve).

(b) Modified Euler (interior of curve).

(c) Backward Euler (exterior of curve).

(d) Runge-Kutta 4 (interior of curve).

Figure 4.1: Stability regions of various numerical integration methods in the complex plane.

4.1.1. Backward Euler

The Backward Euler method is an implicit method which takes more time to solve the equations than Forward Euler (explicit method) for example, but has the advantage that it is usually more numerically stable for solving a stiff equation and therefore a larger step size can be used. The implicit backward Euler method is defined by [1]

$$\mathbf{Y}^{n+1} = \mathbf{Y}^{n} + h\mathbf{f}(t^{n+1}, \mathbf{Y}^{n+1}), \text{ where } \mathbf{Y}^{n+1} \approx \mathbf{Y}(t^{n+1}) \tag{4.1}$$

Even though the method is numerically quite stable, the step size is chosen adaptively, meaning that it adapts to the truncation error. An approximation for this truncation error is given by

$$\tau_{j+1} = ||\mathbf{Y}_{j+1} - \tilde{\mathbf{Y}}_{j+1}||_{\infty}, \tag{4.2}$$

where $\mathbf{Y}$ and $\tilde{\mathbf{Y}}$ are two different numerical methods. In our problem we compute the truncation error for the precipitate number density N and precipitate mean diameter R separately. To use this adaptive step size, we need a second numerical method to compare it to our Backward Euler method. We choose the Backward Euler method itself for this, but using two smaller step sizes $\frac{h}{2}$ leading to two solutions, at time$(j) + \frac{h}{2}$ and time$(j) + \frac{h}{2} + \frac{h}{2}$ =time$(j) + h$, which we can then compare to the one step Backward Euler at time$(j) + h$. Subsequently we use a tolerance parameter to determine whether we accept or reject our approximation $\mathbf{Y}_{j+1}$:

$$\text{TOL} = \text{percentage} \cdot ||\mathbf{Y}_{j+1}||_{\infty}. \tag{4.3}$$

This leads to Algorithm 4.1, where the parameters h_{start}, α β, TOL and t_{end} are set by the user.

4.1.2. Backward Euler combined with Forward Euler

Since the differential equation for N, the precipitate number density, is more easy than the differential equation for R, the precipitate radius, and the differential equation for R has a singularity making it unstable, we use a combination of the Backward Euler method for the differential equation for R and the Forward Euler method for N, which leads to Algorithm 4.2 for each time step. Again we will use the method itself with two half time steps and one whole time step for finding an approximation of the truncation error. Again we compute the truncation error for N and R separately.

---

[1] Note that the new time is also found in this step.

Algorithm 4.1: Euler Backward with adaptive time step algorithm

```
Set h = hstart;
while time(j)+h < tend
    Compute $\tilde{Y}_{j+1/2}$;
    Compute $\tilde{Y}_{j+1/2+1/2}$ based on $\tilde{Y}_{j+1/2}$;
    Compute $Y_{j+1}$; %Use $\tilde{Y}_{j+1/2+1/2}$ as initial value for the BE method
    Compute $\tau_{j+1}$;
    if $\tau_{j+1} > \beta\cdot$ TOL
        Reject $Y_{j+1}$;
        Set h = h/2;
    elseif $\tau_{j+1}$ > TOL
        Accept $Y_{j+1}$;
        Set h = h$\cdot 0.9\cdot(\mathrm{TOL}/\tau_{j+1})^{1/2}$;
        Set j = j+1;
    elseif $\tau_{j+1}$ > TOL/$\alpha$
        Accept $Y_{j+1}$;
        Set j = j+1;
    else
        Accept $Y_{j+1}$;
        Set h = h$\cdot 0.9\cdot(\mathrm{TOL}/\tau_{j+1})^{1/2}/\alpha$;
        Set j = j+1;
    end
end
```

Algorithm 4.2: Euler Backward and Forward Euler with adaptive time step algorithm

```
Set h = hstart;
while time(j)+h < tend
    % Compute using Forward Euler
    Compute $\tilde{N}_{j+1/2}$;
    Compute $\tilde{N}_{j+1/2+1/2}$ based on $\tilde{N}_{j+1/2}$;
    Compute $N_{j+1}$;
    Compute $\tau^N_{j+1}$;
    % Compute using Backward Euler
    Compute $\tilde{R}_{j+1/2}$;
    Compute $\tilde{R}_{j+1/2+1/2}$ based on $\tilde{R}_{j+1/2}$;
    Compute $R_{j+1}$;;  %Use $\tilde{R}_j$ as initial value for the BE method
    Compute $\tau^R_{j+1}$;

    if $\tau^N_{j+1} > \beta\cdot$ TOL && $\tau^R_{j+1} > \beta\cdot$ TOL
        Reject $N_{j+1}$ && $R_{j+1}$;
        Set h = h/2;
    elseif $\tau^N_{j+1}$ > TOL && $\tau^R_{j+1}$ > TOL
        Accept $N_{j+1}$ && $R_{j+1}$;
        Set h = max(h$\cdot 0.9\cdot(\mathrm{TOL}/\tau^N_{j+1})^{1/2}$,h$\cdot 0.9\cdot(\mathrm{TOL}/\tau^R_{j+1})^{1/2}$);
        Set j = j+1;
    elseif $\tau_{j+1}$ > TOL/$\alpha$
        Accept $N_{j+1}$ && $R_{j+1}$;
        Set j = j+1;
    else
        Accept $N_{j+1}$ && $R_{j+1}$;
        Set h = max(h$\cdot 0.9\cdot(\mathrm{TOL}/\tau^N_{j+1})^{1/2}/\alpha$,h$\cdot 0.9\cdot(\mathrm{TOL}/\tau^R_{j+1})^{1/2}/\alpha$);
        Set j = j+1;
    end
end
```

4.1.3. MATLAB Ode15s

The MATLAB Ode15s method is based on the 1-5$^{\text{th}}$ Backward Differentiation Formulas (BDFs), which are a family of implicit methods for the numerical integration of ordinary differential equations. They are linear multi-step methods that, for a given function and time, approximate the derivative of that function using information from already computed times, thereby increasing the accuracy of the approximation (Wikipedia (2016a)). These methods are especially used for the solution of stiff differential equations, indicated in the MATLAB method by the *s*. However, by default MATLAB uses the Numerical Differentiation Formulas (NDFs), which are based on BDF methods (Alberdi Celaya et al. (2014)). This NDF method anticipates a backward difference of order $(k+1)$ when working in order k, which has a positive effect on the local truncation error. This means that the NDF methods are more accurate than the BDF methods (with a same step size), but also a bit less stable. Applying the NDF methods instead of the BDF methods is done for order $k = 1,..,4$, since for higher orders it is inefficient. The Ode15s method starts by solving with order 1 and by the maximum order. The maximum order (*MaxOrder*) is 5 by default, but can be changed by giving a different input for *MaxOrder* to the MATLAB function. In Figure 4.2 the stability regions (exterior of curves) of the 1-5$^{\text{th}}$ BDF methods are given. The colours of the lines correspond to the order of the BDF method: blue = 1$^{\text{st}}$, red = 2$^{\text{nd}}$, green = 3$^{\text{rd}}$, pink = 4$^{\text{th}}$, yellow = 5$^{\text{th}}$. If we zoom in on the origin (Figure 4.3), we see that the stability regions of the first order (blue) and second order (red) BDF method include the entire left half complex plane. This is called A-stable and also holds for the first and second order NDF method. Increasing the order of the formula, means decreasing the stability. There is a class of stiff problems (stiff oscillatory) that is solved more efficiently if MaxOrder is reduced (for example to 2) so that only the most stable formulas are used (Mathworks (2016)).

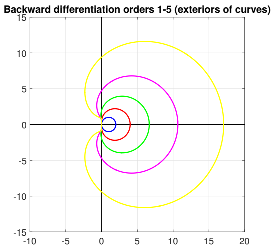

Figure 4.2: Stability regions (exterior of the curves) for the 1-5$^{\text{th}}$ BDF methods in the complex plane.

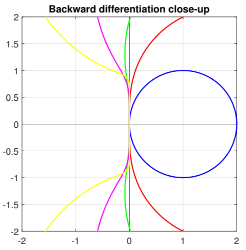

Figure 4.3: Zoomed in stability region (exterior of the curves) for the 1-5$^{\text{th}}$ BDF methods in the complex plane.

More details on this MATLAB Ode15s function can be found in Alberdi Celaya et al. (2014).

4.2. Non-linear equations

For each time step of our numerical time integration method we calculate the activation energy ΔG^*, critical radius R^* and matrix concentrations that depend on the amount and size of precipitates and therefore depend on time. For the critical radius and activation energy, Equation (3.7) cannot be solved analytically so we have to use a numerical method. Various methods can be used for this, but we need one which converges fast to keep the simulation fast. The implementation done by Tata Steel (Kranendonk (2005)) uses the Ridders method, which converges superlinearly. An alternative is the Newton-Raphson method which converges quadratically most of the time. A disadvantage of this method is that the derivative of the function is needed, which is not an objection in our case because of the simplicity of the function. Another disadvantage is that the method is not very robust, meaning that a wrongly chosen initial value could lead to divergence of the method. However, also this is not an objection in our case because we have a good initial guess: the critical radius and activation energy for homogeneous nucleation. For other non-linear equations that come forward during the implementation, we weigh the advantages and disadvantages of each solving method again and choose the one that fits best.

Besides the non-linear equations in the model itself, the solving of the differential equations also results in a set of non-linear equations, since we use an implicit integration method and our right hand side $\mathbf{f}$ is non-linear. To solve this non-linear equation a variety of (root finding) methods could be used. Using Newton-Raphson for the Backward Euler iteration could be an option, except that we would have to find the derivative

of the right-hand side of our differential equations, which is difficult. A different option could be to use the bisection method, but this method has some disadvantages. Since we have two differential equations, we need a two-dimensional bisection method, which is quite difficult. Also, the bisection method converges slowly, which could lead to a slow integration method.
We believe the best option in this case would be to use a fixed point method called Picard's iteration method, since it is an easy method which does not depend strongly on the initial guess as other methods do. The fixed point method states we can find a fixed point p of a function g if we start with an initial point p_0 and use the iteration p_n by $p_n = g(p_{n-1})$. If this sequence converges to p and g is continuous it holds that $p = g(p)$ and we have found a fixed point p (Vuik et al. (2015)). Going back to equation (4.1), we find

$$\begin{aligned}\mathbf{Y}_{k+1}^{n+1} &= g(\mathbf{Y}_k^{n+1}), \quad k = 0, 1, \ldots \\ &= \mathbf{Y}_k^n + h\mathbf{f}(\mathbf{t}^{n+1}, \mathbf{Y}_k^{n+1})\end{aligned}$$

as our Picard's iteration step. In this iteration k indicates the fixed point iteration and n the time step.

5

Computational issues

During the first simulations, using the algorithms described in the previous chapter, a number of computational issues arouse. In this chapter, these issues will be explained and solutions are opposed. After applying the improvements mentioned in this chapter, simulations are done of which the results can be found in Chapter 6.

5.1. Interface concentrations

During the first simulations, we found a negative growth rate. As Zurob also noticed in his PhD thesis (Zurob (2003)) this is mainly because of the Gibbs-Thomson equation for homogeneous nucleation used to approximate the interface concentrations. If the mean radius of the precipitates is smaller than the critical radius for homogeneous nucleation, the Gibbs-Thomson equation results in a negative growth rate. A solution proposed by Zurob (2003) was to calculate the interface concentrations by solving for the interface concentration Nb in Equation (3.7). We start with the growth rate (Equation (3.8)) for each element X separately:

$$R' = \frac{dR}{dt} = \frac{D_{eff}}{R}\frac{C_X^M - C_X^R}{C_X^P - C_X^R},$$

equivalently

$$C_X^R = \frac{D_{eff}C_X^M - R'RC_X^P}{D_{eff} - R'R}. \tag{5.1}$$

This results in three equations (for Nb, N and C) with four unknowns: R', C_{Nb}^R, C_N^R and C_C^R, for which generally there are no solutions found. For the fourth equation Zurob et al. (2002) proposed to calculate the concentrations at the interface from the solubility product, corrected for the Gibbs-Thomson effect at dislocations. We start from Equation (3.7):

$$\frac{d(\Delta G)}{dR} = 4\pi R^2\Delta g_v + 8\pi R\gamma - \frac{\mu b^2}{2\pi(1-\nu)}(\ln(R/b)+1) - \frac{\mu b^2}{5} = 0.$$

This equation involves the free energy change attending nucleation Δg_v, a function depending on the product of interface concentrations. Rewriting Equation (3.7), we find

$$\Delta g_v = -\frac{2\gamma}{R} + \frac{\mu b^2}{8\pi^2(1-\nu)R^2}(\ln(R/b)+1) + \frac{\mu b^2}{20\pi R^2}.$$

Using the definition of Δg_v (Equation (3.4)) and replacing the matrix product with the interface product, we get

$$-\frac{R_g T}{v_{m,NbCN}}\ln\left(\frac{\text{interface product}}{\text{solubility product}}\right) = -\frac{2\gamma}{R} + \frac{\mu b^2}{8\pi^2(1-\nu)R^2}(\ln(R/b)+1) + \frac{\mu b^2}{20\pi R^2}, \tag{5.2}$$

where

$$\text{interface product} = wt\%Nb^R(wt\%C^R)^x(wt\%N^R)^{1-x}.$$

Combining the three equations for the growth rates (Equation (5.1)) with the equation for the energy changes (Equation (5.2)), results in four equations with four unknowns: R', C^R_{Nb}, C^R_N and C^R_C, which we can solve.

We use the bisection method to solve the following equation:

$$\frac{\text{interface product}}{\text{solubility product}} - \exp\left(-\frac{v_{m,NbCN}}{R_g T}\left(-\frac{2\gamma}{R} + \frac{\mu b^2}{8\pi^2(1-\nu)R^2}(\ln(R/b)+1) + \frac{\mu b^2}{20\pi R^2}\right)\right) = 0, \tag{5.3}$$

which is a function of R' via the interface product (the interface concentrations depend on R' via Equation (5.1)). Using this bisection method, we get back the growth rate R', and thereby via Equation (5.1) the interface concentrations.

To analyse why this is an improved approximation of the interface concentrations, we rewrite Equation (5.3), and retrieve the Gibbs-Thomson equation for homogeneous nucleation (Equation (3.9)):

$$\begin{aligned}\frac{\text{interface product}}{\text{solubility product}} &= \exp\left(-\frac{v_{m,NbCN}}{R_g T}\left(-\frac{2\gamma}{R} + \frac{\mu b^2}{8\pi^2(1-\nu)R}(\ln(R/b)+1) + \frac{\mu b^2}{20\pi R^2}\right)\right),\\ &= \exp\left(\underbrace{\frac{2\gamma v_{m,NbCN}}{R_g T}\frac{1}{R}}_{\substack{\text{homogeneous}\\ \text{Gibbs-Thomson}}} - \frac{v_{m,NbCN}}{R_g T}\left(\frac{\mu b^2}{8\pi^2(1-\nu)R^2}(\ln(R/b)+1) + \frac{\mu b^2}{20\pi R^2}\right)\right).\end{aligned}$$

The interface concentrations found by the above described process are therefore also corrected for the Gibbs-Thomson effect for heterogeneous nucleation at dislocations and not just for homogeneous nucleation.

5.2. Coarsening function

During the implementation it became clear that the value of the coarsening function chosen in Chapter 3 gave a value of 2 at time zero (when choosing $N = 0$ and $R = 0$ as initial conditions), whereas we require the coarsening function to take values between 0 and 1. The coarsening function can be rewritten as

$$\begin{aligned}F_c &= 1 - \operatorname{erf}\left(4\left(\frac{R}{R_0}\ln\left(\frac{C^M_{Nb}}{C^{Eq}_{Nb}}\right) - 1\right)\right),\\ &= 1 - \operatorname{erf}\left(4\left(\frac{R}{R^*_h} - 1\right)\right),\end{aligned}$$

where R^*_h is the critical radius for homogeneous nucleation. Updating this function, using the critical radius for heterogeneous nucleation could already be an improvement, but will not solve the problem that the coarsening function returns values between 2 and 0, as shown in Figure 5.1a.

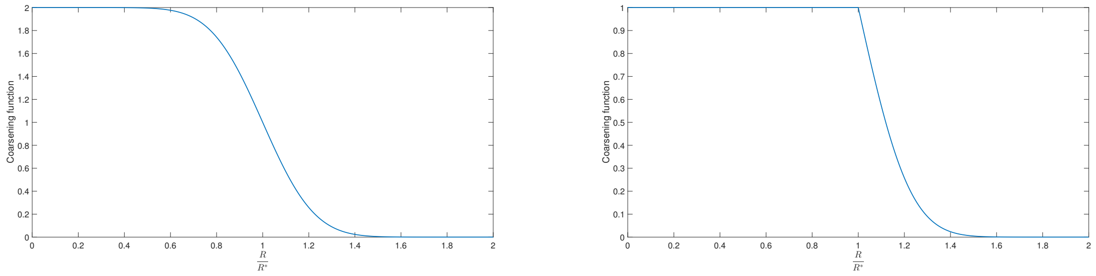

(a) Deschamps' coarsening function from Deschamps and Brechet (1999).

(b) Adaption of Deschamps' coarsening function by Kranendonk (2005).

Figure 5.1: Plot of the coarsening function F_c against R/R^*, with R^* the critical radius for heterogeneous nucleation.

To solve these problems, Kranendonk (2005) improved the function by setting restrictions on the value of the function:

- If the mean radius is below the critical radius ($R < R^*$), the coarsening function should return 1, leading to the following restriction:
  If $a = 4\left(\frac{R}{R^*} - 1\right) < 0$, let $a = 0$, so that $F_c = 1 - \text{erf}(0) = 1$.
- If the volume fraction of the system is too small, say below 10% of the maximum volume fraction, no coarsening should be present and F_c should be 0.

When applying these restrictions to the implementation, the coarsening function looks like Figure 5.1b. As can be seen, it returns values between 0 and 1, as necessary. In Chapter 6 of this literature study we will introduce some other coarsening functions and compare them (and the way they influence the resulting solution).

5.3. Unstable solutions

As described in Chapter 4 we use an adaptive step size in our numerical methods. Unfortunately this gave some problems due to the large instability of the physical model. When the solution is correct, the step size is increased, but during the simulation the step size eventually got too large. At that point the concentrations got negative and the algorithm stopped. To prevent this from happening, we set a bound on the step size. Also, when the computation is precisely good ($\tau_{j+1} = 0$) the algorithm stopped, since the new step size is found by a division by τ_{j+1}. We adjusted this by setting the step size back to the starting step size *hstart* when $\tau_{j+1} = 0$. This was necessary since sometimes the step size can get quite large, it then may occur that the last part of the time interval is skipped, as illustrated by the yellow block in Figure 5.2. In this case, we adjust the step size to the remainder of the time interval.

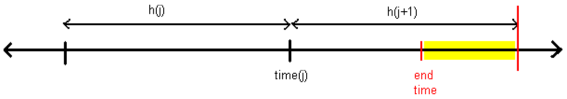

Figure 5.2: Illustration of the time steps at the end of the time interval.

Applying the above mentioned adjustments to our algorithm, we came to Algorithm 5.1 (a general description which can apply to both the Backward Euler and the Backward Euler with Forward Euler method).

Algorithm 5.1: Adjusted algorithm (general version) with a different step size selection

```
Set N=1;
Set h = hstart;
while time(j)+h < tend
    Compute $\tilde{Y}_{j+1}$;
    Compute $Y_{j+1}$;
    Compute $\tau_{j+1}$;
    if $\tau_{j+1} > \beta\cdot$ TOL
        Reject $Y_{j+1}$;
        Set h = h/2;
    elseif $\tau_{j+1} >$ TOL
        Accept $Y_{j+1}$;
        Set h = min($h\cdot 0.9\cdot(\mathrm{TOL}/\tau_{j+1})^{1/2}$,500);
        while time(j+1)+h > tend
            Set h = h/2;
        end
        Set j = j+1;
    elseif $\tau_{j+1} >$ TOL/$\alpha$
        Accept $Y_{j+1}$;
        Set j = j+1;
    else
        Accept $Y_{j+1}$;
        if $\tau_{j+1} == 0$
            Set h = hstart;
        else
            Set h = min($h\cdot 0.9\cdot(\mathrm{TOL}/\tau_{j+1})^{1/2}/\alpha$,500);
        end
        while time(j+1)+h > tend
            Set h = h/2;
        end
        Set j = j+1;
    end
end
```

6

Numerical Results

As described in Chapter 4 we use three different integration methods, which we will compare in Section 6.1. We will compare different coarsening functions and their performance in the simulation in Section 6.2. Finally in Section 6.3 we will study the influence of the initial values on the evolution of the precipitates and on the performance of the algorithm. During the simulations, we use the standard setting as described in Appendix D and the conversion formulas from Appendix C. For the parameters, we use the configuration as given in Table 6.1[1] and Table 6.2[2], and an alloy (Table 6.3) that was also used in the simulations done by Kranendonk (2005) and Zurob et al. (2002), enabling a comparison of the algorithms and of their results. When comparing the effects of the initial values, we start with the standard setting and compare the new result to it.

Table 6.1: Precipitation parameters used in the simulations.

Parameter	Value	Unit
T	1123.15 (850 °C)	K
R_g	8.31441	J/(K mol)
ρ	3.27×10^{14}	$1/\mathrm{m}^2$
k_B	1.38×10^{-23}	J/K
ν	0.293	
F	1.32×10^{-3}	
N_a	6.022142×10^{23}	1/mol
$v_{m,NbC}$	13.39×10^{-6}	$\mathrm{m}^3/\mathrm{mol}$
$v_{m,NbN}$	12.72×10^{-6}	$\mathrm{m}^3/\mathrm{mol}$
b	2.53144×10^{-10}	m
$N(0)$	1×10^{10}	$1/\mathrm{m}^3$
$R(0)$	R^*	m

Table 6.2: Numerical parameters used in the simulations.

Parameter	Value	Unit
α_n	1.05	
h_{start}	1×10^{-5}	s
TOL	1×10^{-5}	
N_{max}	75	
α	2	
β	100	
t_{start}	0.001	s
t_{end}	12040	s

Table 6.3: Alloy composition of alloy N1 used in the simulations in weight percentages (Kranendonk (2005)).

C	Si	Mn	P	S	Nb	Al	N	Fe
0.076	0.06	1.34	0.0058	0.0026	0.03	0	0.0061	98.4795

6.1. Integration methods

We compare the three integration methods from Chapter 4, checking the time it took for the method to solve the problem, the number of iterations and the quality of the resulting solution (compared to those retrieved by Kranendonk (2005)). In Figure 6.1 the simulation results using the different integration methods are shown. Table 6.4 shows the duration of the simulation, the number of iterations and the number of time steps for each integration method. For the Backward Euler and the combination method, the number of iterations is the total number of method iterations, so also includes rejections of a solution and reducing the time step. The number of iterations in the MATLAB Ode15s method is the number of successful steps.

---

[1] The temperature, time and composition dependent parameters are found in Appendix D.

[2] The function of each numerical parameter can be found in the nomenclature.

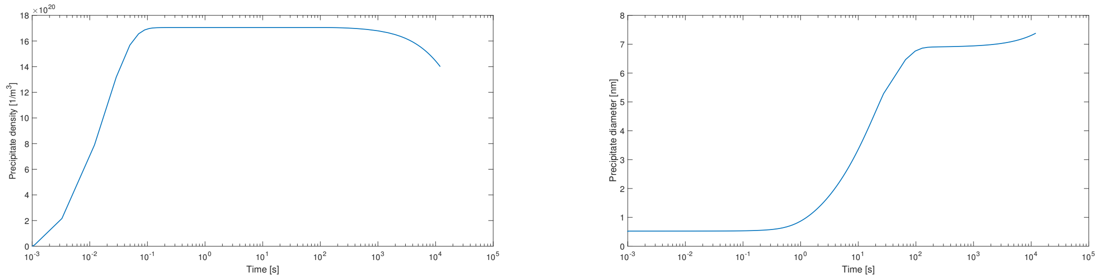

(a) Backward Euler - Number density. (b) Backward Euler - Mean diameter.

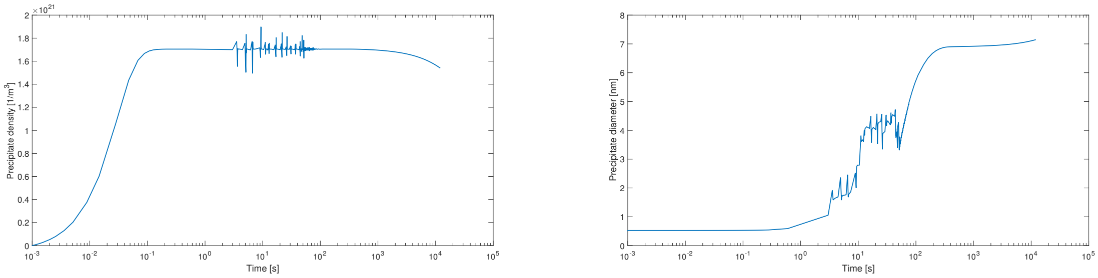

(c) Backward Euler and Forward Euler - Number density. (d) Backward Euler and Forward Euler - Mean diameter.

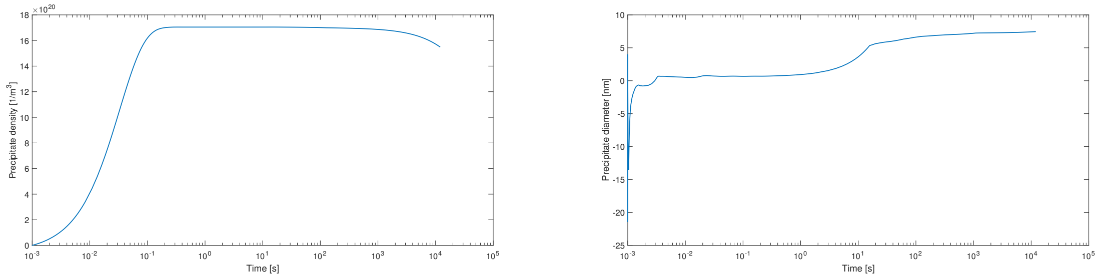

(e) ODE15s - Number density. (f) ODE15s - Mean diameter.

Figure 6.1: Simulation results using the standard settings from Appendix D and for the MATLAB Ode15s: RelTol = 1×10^{-3}, AbsTol = 1×10^{-7}, NonNegative = N, Refine = 4.

Table 6.4: Overview of the different integration methods by time, number of iterations and error.

Method	Computer time (s)	#Iterations	#Time steps
Backward Euler	63.0.14190	1623	316
Backward Euler & Forward Euler	66.523643	754	446
Ode15s	2.324776	109 (successful steps)	437

The overview in Table 6.4 shows that the Backward Euler method is slightly faster then the combined Backward Euler and Forward Euler method, but that the MATLAB Ode15s is by far the fastest method. Using the Backward Euler with Forward Euler method was mainly tested to speed up the simulation, since implicit methods are known to be slow. However, this does not seem to work, even though the number of iterations in the combined method is lower. This is due to the number of time steps made by the combination method, which is higher then the number of time steps used by the Backward Euler method.

Using the duration of the simulations as a guideline, one would choose the MATLAB Ode15s method, but looking at the results in Figures 6.1e and 6.1f we see it returns physically impossible values. The MATLAB Ode15s method predicts negative values for the mean precipitate radius at very early times, which is physically unacceptable. In Figure 6.2 the results are plotted with the same vertical axes, as has been used for the two other methods. Although this result is globally similar to the result of the Backward Euler the oscillations in the results of the MATLAB routine have no physical explanation. Therefore this method will not be used in further simulations.

Using the Backward Euler with Forward Euler method also results in oscillations as shown in Figures 6.1c and 6.1d. We find that at some moment the precipitate density increases to above the plateau, which results in an oscillatory precipitate diameter. The volume fraction as a function of time as predicted by the Backward Euler with Forward Euler is given in Figure 6.3. We see that once the volume fraction is slightly above zero (0×10^{-4}), the oscillations start. When using only the Backward Euler method no such oscillations are found, showing that using the forward step in the equation for the number density destabilises the algorithm. Therefore this method will not be used in further simulations.

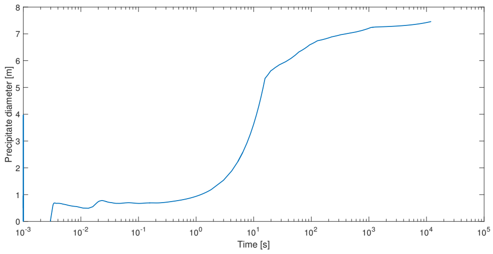

Figure 6.2: Precipitate mean diameter using MATLABs Ode15s method and axes from the other methods.

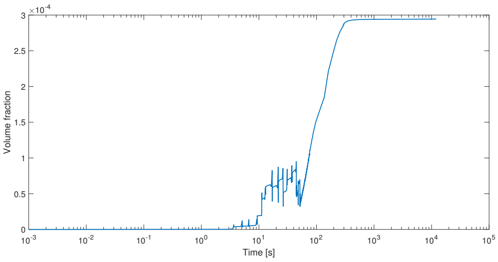

Figure 6.3: Volume fraction in time using the Backward Euler with Forward Euler method.

Even though the simulation done with the Backward Euler method result in a small bend at the beginning of precipitate density (Figure 6.1a), it still gives the best results compared to the other two methods and therefore we will use the Backward Euler as our integration method during the simulation for the other calculations. When we compare the results from the simulation using this Backward Euler method (Figures 6.1a and 6.1b) and the simulation done by Tata steel (Kranendonk (2005), Runge-Kutta 4) we find Figure 6.4. The results of the two simulation methods look quite the same, but do have some small deviations with respect to each other. These deviations can be explained by the differences between the two implementations, of which an overview is given in Table 6.5. Since the deviations are small, and the model of Kranendonk (2005) was fitted on experimental data and the model of Zurob et al. (2002), it is safe to assume that our model predicts the experimental data accurately.

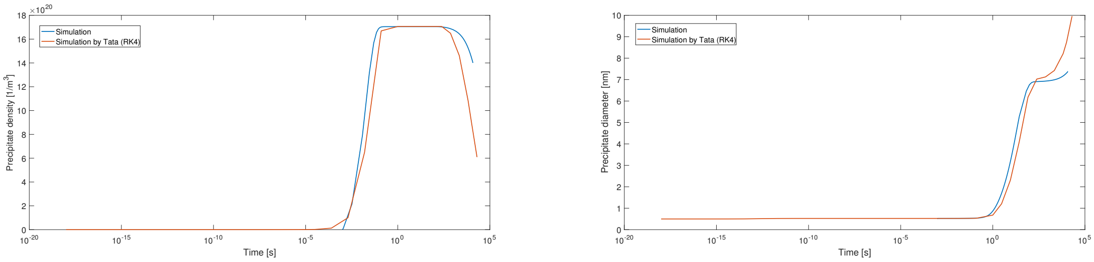

(a) Precipitate number density.

(b) Mean diameter.

Figure 6.4: Simulation results using BE compared to simulation by Tata Steel using Runge-Kutta 4.

Table 6.5: Differences in implementation between this literature study and Tata Steel

	Literature study	Tata Steel
Integration method	Backward Euler	Runge-Kutta 4
Lattice constant	$10^{-9} \times (0.36306 + 0.078x_c) \cdot$ $(1 + (24.9 - 50x_c)(T - 1000) \times 10^{-6})$	3.6444×10^{-10}
Calculation interface concentration (IC)	Variable C and N IC	C and N IC equal to matrix concentration
Differential equation for R during coarsening	$\frac{4}{27} \frac{C_{Nb}^{Eq}}{C_{Nb}^{P} - C_{Nb}^{Eq}} \frac{R_0 D}{R^2}$	$\frac{D_{eff}}{R} \frac{0.01(wt\%Nb^{R} - wt\%Nb^{R27/23})}{wt_{Nb}^{P} - 0.01\, wt\%Nb^{Eq}}$ (based on Zurob (2003))
Unit	Concentrations	Weight percentages / molar fractions

6.2. Coarsening function

As described in Chapter 5 the original coarsening function by Deschamps and Brechet (1999) had to be adjusted to to fullfil the requirements (namely $0 \leq F_c \leq 1$). However, by setting such restrictions, the coarsening function looses its original properties. Also, this coarsening function fails to describe precipitate dissolution, an effect we also would like to be able to describe later on.

Choosing a different coarsening function, which has the properties we want without setting restrictions on the value of variables in the function would be preferable. We choose different coarsening functions and compare them to the coarsening function chosen by Kranendonk (2005). These coarsening functions must meet the requirement of returning values between 0 and 1, where it returns 1 during pure coarsening and 0 during pure nucleation. The following coarsening functions are compared:

1. The original coarsening function with the heterogeneous critical radius and restrictions proposed by Kranendonk (2005):

$$F_c = 1 - \mathrm{erf}\left(4\left(\frac{R}{R^*} - 1\right)\right), \quad \text{Figure 5.1b.}$$

2. A coarsening function based on the current volume fraction (f_v) and the equilibrium volume fraction corrected by the Gibbs-Thomson effect ($f_{v,GT}$) by Perrard et al. (2007):

$$F_c = \sup\left[1 - 100\left(\frac{f_v}{f_{v,GT}^{eq}} - 1\right)^2, 0\right], \quad \text{Figure 6.5.}$$

3. A coarsening function based on the heterogeneous critical radius by Perez et al. (2008), with restrictions:

$$F_c = \begin{cases} 1 - 1000\left(\frac{R}{R^*} - 1\right)^2, & \text{in } \Omega \\ 0, & \text{else} \end{cases},$$

where $\Omega = \{0.99R^* < R < 1.01R^*$ and volume fraction $> 0.1 *$ maximum volume fraction$\}$, Figure 6.6.

4. A coarsening function based on the saturation, corrected for saturation above 1:

$$F_c = \sup\left[2 - \text{saturation}(t), 0\right], \quad \text{Figure 6.7.}$$

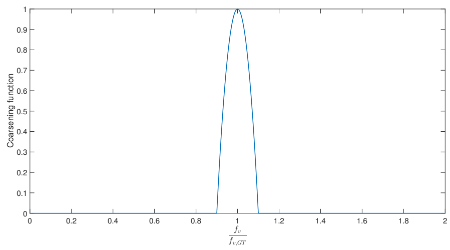

Figure 6.5: Coarsening function by Perrard et al. (2007).

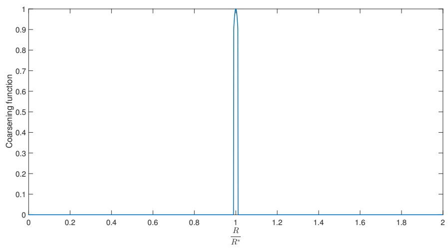

Figure 6.6: Coarsening function by Perez et al. (2008).

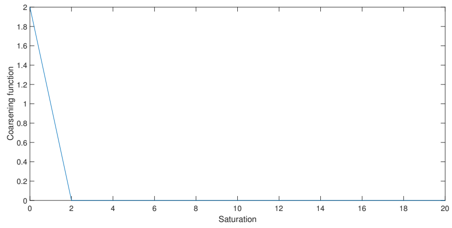

Figure 6.7: Saturation based coarsening function.

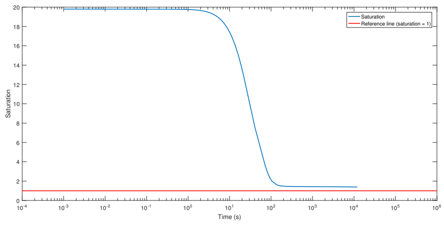

Figure 6.8: The saturation in time, together with a reference line at saturation = 1 (the limit of the saturation as time goes to infinity).

Unfortunately, it soon became clear that the saturation based coarsening function would not give the desired result. Since the saturation must go to one for time to infinity, we used this to define our coarsening function. However, if we plot the saturation found using Backward Euler with Picard and the coarsening function by Kranendonk (2005), we find Figure 6.8. It seems that the saturation does indeed approach one, but never reaches this point, resulting in the fact that the coarsening function never equals 1, and therefore pure coarsening never takes place. Comparing this to the other coarsening functions found in Figure 6.9, we see that those functions do reproduce pure coarsening ($F_c = 1$). Therefore the saturation based coarsening function will not be used.

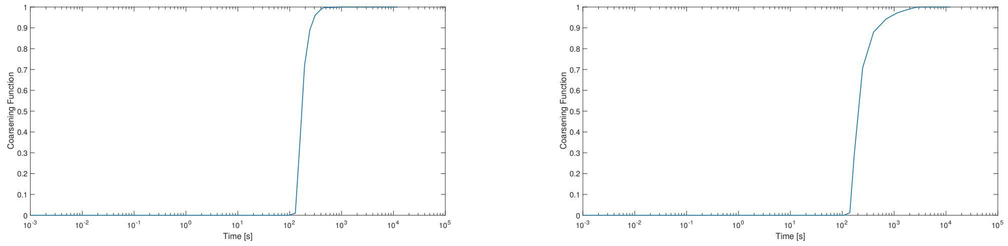

(a) By Deschamps and Brechet (1999).

(b) By Kranendonk (2005).

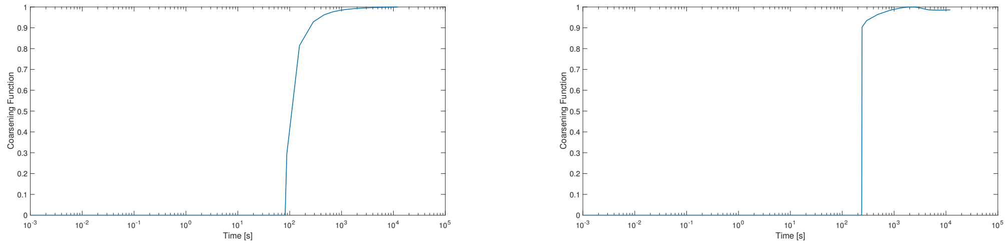

(c) By Perrard et al. (2007).

(d) By Perez et al. (2008).

Figure 6.9: Coarsening functions in time (using Euler Backward with Picard in the implementation).

When we look at the results in Figure 6.9, and specifically at Figure 6.9d, we see that the coarsening function by Perez et al. (2008) drops below one after some time. It is unclear why this happens and is physically incorrect for isothermal calculations. Furthermore, the coarsening functions by Deschamps and Brechet (1999) (Figure 6.9a), by Kranendonk (2005) (Figure 6.9b) and by Perrard et al. (2007) (Figure 6.9c) have the same behavior, but slightly differ in the way they start (from $F_c = 0$ to $F_c \neq 0$) and the way they reach the top (close to $F_c = 1$). However, the differences between the coarsening functions are so small, that they will not strongly influence the final results.

We choose to use the coarsening function by Perrard et al. (2007) in our simulations, since that is the only coarsening function that can also describe precipitate dissolution ($f_v > f_v^{Eq}$) and does not have additional restrictions when implemented. An additional benefit of this function is that it is checked to be valid for both isothermal and non-isothermal heat treatments (Perrard et al. (2007)).

6.3. Variable variation

To test the model and the adaptivity of the implementation, we choose multiple initial values and analyse the effect it has on the precipitate number density and the mean radius. First we will vary the initial precipitate number density and mean radius to see whether the starting precipitate number density has large effects on the nucleation rate of the precipitates. Second we will vary the temperature homogeneously and compare the results. We also tested a non-isothermal condition by introducing a temperature curve, to see the effect of increasing temperature during the nucleation and growth of precipitates. Thirdly, we will simulate for different dislocation densities. Finally we compare the effect of different chemical compositions (alloys) on precipitate evolution.

6.3.1. Initial precipitate number density and mean radius

In this section we will compare the results using different initial values for the precipitate number density N and the mean radius R. We will simulate the nucleation and growth for three different initial densities and mean radiuses. For $T = 850$ °C and $\rho = 3.27 \times 10^{14}$ m^{-2} we have a maximum volume fraction of 3.2267×10^{-4} and a initial critical radius of 2.49×10^{-10}. For each initial value we find the initial volume fraction via

$$f_v = \frac{4}{3}\pi N R^3,$$

and compare it to the maximum volume fraction. On $t = 0$[1], we set:

Table 6.6: Various initial values chosen in the simulations.

Setting	Precipitate number density N	Precipitate mean radius R	Initial volume fraction f_v^{Init}
(a)	0	R^*	0
(b) - original setting in previous simulations	1×10^{10}	R^*	6.49×10^{-19}
(c)	1×10^{21}	R^*	6.49×10^{-8}

For initial setting (a) we start with no precipitates. if there are no precipitates, the radius of those precipitates is free to choose. We set the radius as the critical radius, because once there is one precipitate it must initially have the critical radius. For initial setting (b) we choose a small amount of precipitates to start with. In the previous simulations we saw that the precipitate density had a top level of around 2.5×10^{21}, so a small amount of precipitates would be 1×10^{10} precipitates per m^3. For initial setting (c) we choose the initial precipitate density slightly lower than the maximum we have seen in previous simulations. The initial volume fraction of setting (c) is the closest to the maximum volume fraction, but still orders of magnitude smaller. The results of the simulation using different initial values are given in Figure 6.10.

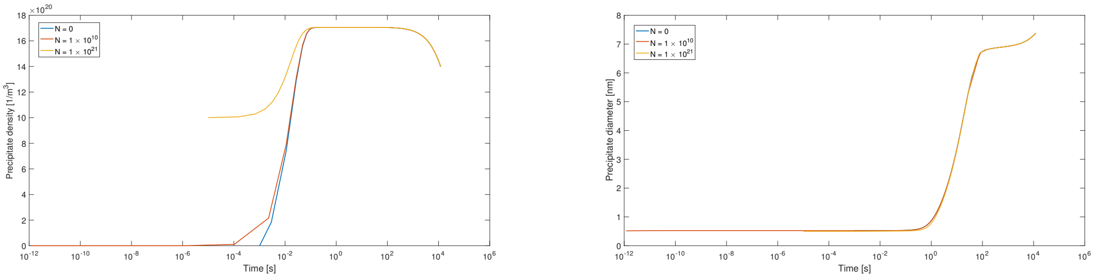

(a) Precipitate number density.

(b) Precipitate mean diameter.

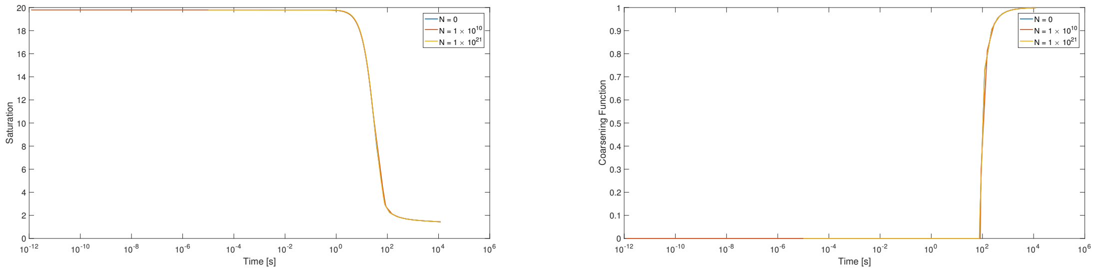

(c) Saturation.

(d) Coarsening function.

Figure 6.10: Simulation results for different initial values at 850 °C and $\rho = 3.27 \times 10^{14}$ m^{-2}.

We note that the difference between the results using initial values setting (a) and initial values setting (b) is very small and can only be seen in the precipitate density for times between 10^{-4} and 10^{-2} seconds. However, the difference between initial values setting (c) and the other other setting is more pronounced for times up to 10^{-2} seconds, even though it only still effects the density. Also we see that when the initial density is chosen

---

[1] Since we would like to change the density and diameter at $t = 0$ we set $t_{start} = 0$ for these simulations.

this high (1×10^{21}) the bend at the beginning has disappeared. This can be explained since the simulation has difficulties around $N \approx 0$ caused by the $1/N$ in the differential equation for the precipitate radius (Equation (3.11)). This is avoided when starting with a high precipitate density (away from zero). Even though there is a clear difference in the beginning, the maximum number density is the same for all initial values and this maximum is reached at almost the same time, irrespective of the initial values. We find that the starting value for the precipitate density has no strong influence on the final results.

6.3.2. Temperature

In this section we will discuss the effect of temperature on the precipitation evolution and investigate the difference in results for isothermal versus non-isothermal temperature schemes. There are some restrictions on the temperatures we choose, since we restrict the simulations to austenite (see Figure 2.3 for the right temperatures), and we must stay below the solvus temperature. The solvus temperature depends on the initial concentrations of the precipitate elements in the alloy and the solubility products of the precipitate elements. It is found by the solving fourth order Equation (3.6) for the temperature. In this equation, we take the initial weight percentage for Nb as the equilibrium weight percentage. For the different alloys that we consider (Table 6.8) we find the solvus temperatures presented in Table 6.7. Alloy N1 will be used in the temperature simulations.

Table 6.7: Solvus temperatures for the different alloys described in Table 6.8.

Alloy	Solvus temperature (°C)
N1	1093.88
N2	1021.21
N4	1240.30

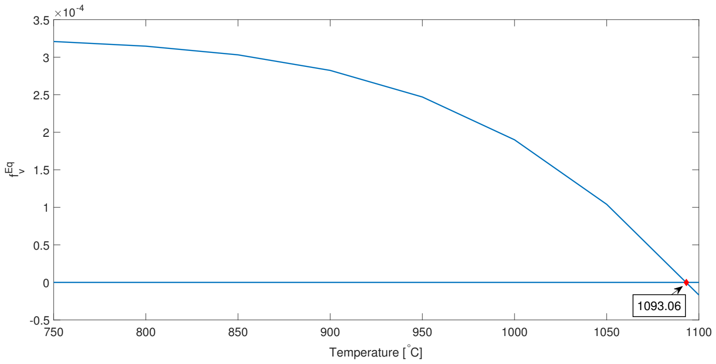

Figure 6.11: Volume fraction against temperature for alloy N1.

Figure 6.11 shows the equilibrium volume fraction as a function of temperature, returning a comparable solvus temperature as found in the analysis with Equation (3.6). For precipitation to take place the temperature should be lower than the solvus temperature.

In the results, the definition of the volume fraction is of great importance. The volume fraction is defined by

$$f_v = \frac{4}{3}\pi N R^3, \tag{6.1}$$

meaning that for a constant volume fraction, a lower precipitate number density (N) leads to larger precipitates (R) and vice versa. This relation will often be used in the rest of this chapter.

Isothermal calculations

Taking the temperature restrictions into account, we choose the following temperatures for the isothermal calculations:

(a) 850 °C, the original temperature from the previous simulations,

(b) 750 °C, below current temperature of 850 °C,

(c) 950 °C, above current temperature of 850 °C.

The results of the simulation using these temperatures are given in Figure 6.16.

Using the results from the isotherm calculations for even more temperatures, we construct a PTT (precipitation-time-temperature) curve, which involves the times when precipitation starts and finishes. This PTT curve can be used to adjust the processes of steel making. It can give a good indication of what type of linear temperature decrease you should use to get the lowest amount of precipitates in the resulting product. We construct the PTT curve, using the following steps, of which the result can be found in Figure 6.12[1].

- The volume fraction of precipitates as a function of time is calculated for a constant temperature. This is indicated in the top picture by the black line.
- Two times on this curve are selected: the time where the volume fraction is 5% of the equilibrium volume fraction and the time where the volume fraction is 95% of the equilibrium volume fraction. These criteria can differ per researcher, some choose respectively 1% and 99% percent as start and end percentages. In the top picture, the equilibrium volume fraction is indicated by the green line, and the 5% and 95% criteria by the red lines. If the time at which the volume fraction is exactly 5% or 95% of the equilibrium volume fraction is not available, interpolation is used to find the specific time.
- The previous step is repeated for various temperatures, in every step leading to two points in the bottom picture. The results are plotted in one diagram, giving two (black) curves as shown in the bottom picture.

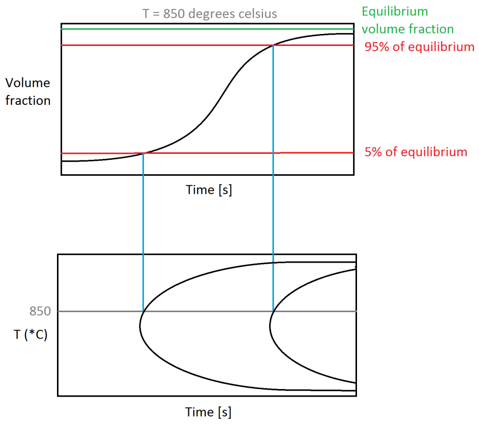

Figure 6.12: Illustration of the construction of a PTT curve.

When we plot the volume fraction for different temperatures, we find Figure 6.13. From literature we know that the temperature has influence on the activation energy and the diffusion coefficient, each with opposite effect: increasing the temperature increases the activation energy, making the chance of forming new nuclei smaller, which leads to a lower nucleation rate. On the other hand, increasing the temperature increases the diffusion coefficient, making it easier to form new nuclei, leading to a higher nucleation rate. In Figure 6.13 we see that until 950 °C the influence from the diffusion coefficient is larger and the nucleation rate increases and at 1000 °C we find the influence from the activation energy is larger, leading to a lower nucleation rate. The hard switch between these situations is unexpected.

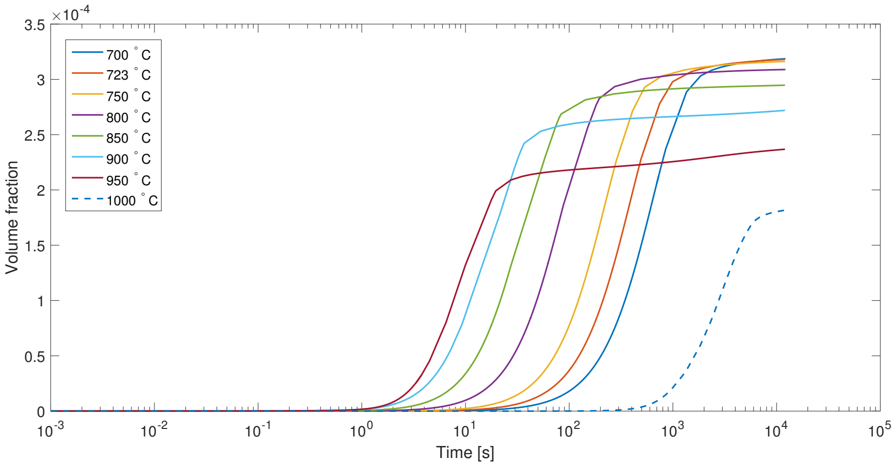

Figure 6.13: Volume fraction in time for different temperatures with $\rho = 3.27 \times 10^{14}\ \mathrm{m}^{-2}$.

When we look at the resulting PTT diagram in Figure 6.14a, the hard switch between 950 °C and 1000 °C is reflected in the non-symmetrical shape of the PTT diagram. In literature most PTT diagrams are plotted

---

[1] When using the PTT curve, take into account that the dislocation density has influence on the curve.

using a base 10 logarithmic scale for the time axis. However, when using such a logarithmic time scale, we find the result is even more non-symmetric (Figure 6.14b). It could be possible that either in literature high temperatures are not considered and the points are fitted to a symmetric curve (not taking the real results into account), or our model is not giving the right results for the PTT diagram. Other causes could be that the equilibrium volume fraction is not correct, as it is not corrected for the Gibbs-Thomson effect, or a large error is made in the interpolation to find the time at which 5% and 95% of the equilibrium volume fraction is reached. When a new model is developed during the continuation of this thesis, a new PTT diagram should be constructed to compare the results and find the cause of the asymmetry. Assuming that our PTT diagram is correct, we can apply various temperature cooling curves (Figure 6.15: indicated by the dotted lines), to see which linear temperature decrease would give the fewest precipitates in the product: in this case the dotted yellow line in Figure 6.15 would be chosen. This is an application of the PTT diagram that is often used in the optimisation of the steel making process.

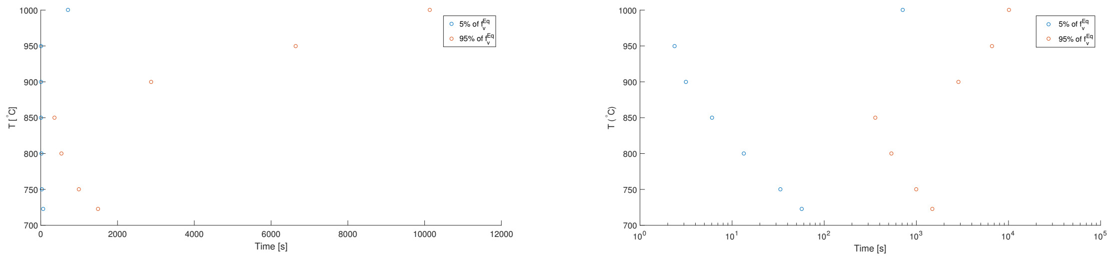

(a) Precipitate-time-temperature curve on a linear time scale.

(b) Precipitate-time-temperature curve on a logarithmic time scale.

Figure 6.14: The precipitate-time-temperature curve with $\rho = 3.27 \times 10^{14}$ m^{-2}.

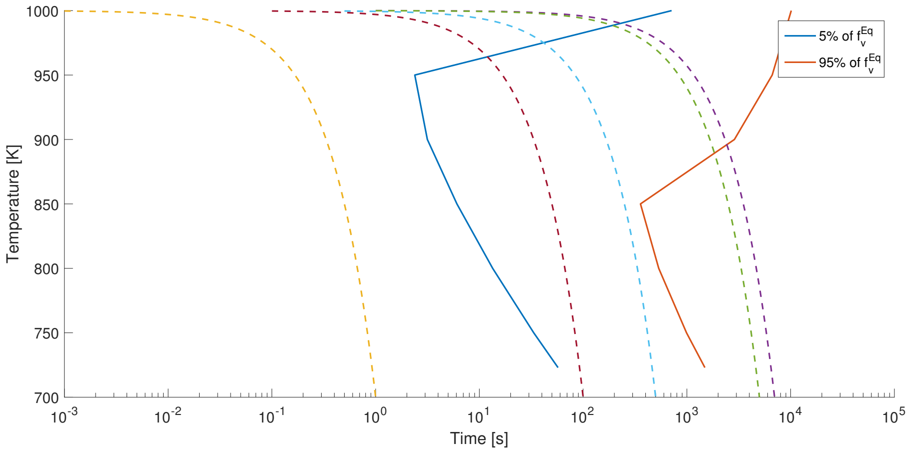

Figure 6.15: Precipitate-time-temperature curve on a logarithmic time scale and various temperature cooling curves.

Using the PTT from Figure 6.14a, we see that results for temperatures above 1000 °C will result in very long simulation times and we will therefore not use this in further simulations. In Figure 6.16 we see that the results at 850 °C have an average time span of precipitation (between 10^{-2} and 10^5 seconds), and results at a slightly higher temperature (950 °C) have a smaller time span of precipitation (between 10^{-1} and 10^4 seconds). In the results of the simulations we furthermore see that the precipitate number density reaches the same maximum plateau (determined by N_{total}, see Equations (3.1) and (3.2)) for 750 °C and 850 °C. The results for 950 °C show that this maximum plateau is not reached, which is due to the competition between nucleation and coarsening at high temperatures. The precipitate mean diameter reflects the same conclusion: for 750 °C and 850 °C the same size of precipitates is reached and for 950 °C the precipitates in the end are larger, due to the constant volume fraction. Increasing the temperature also leads to a lower saturation (Figure 6.16c) and earlier coarsening (Figure 6.16d).

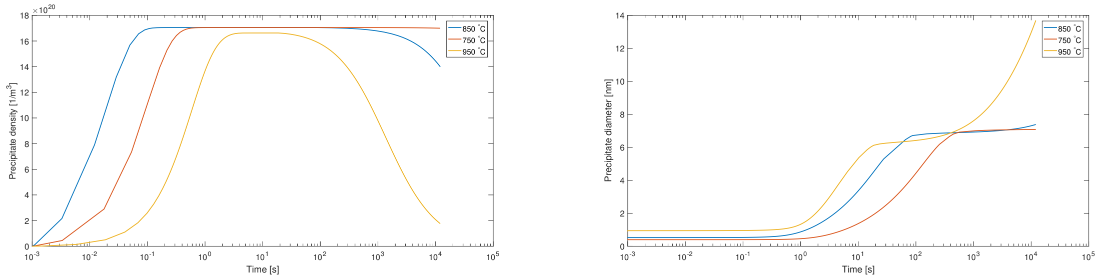

(a) Precipitate number density.

(b) Precipitate diameter.

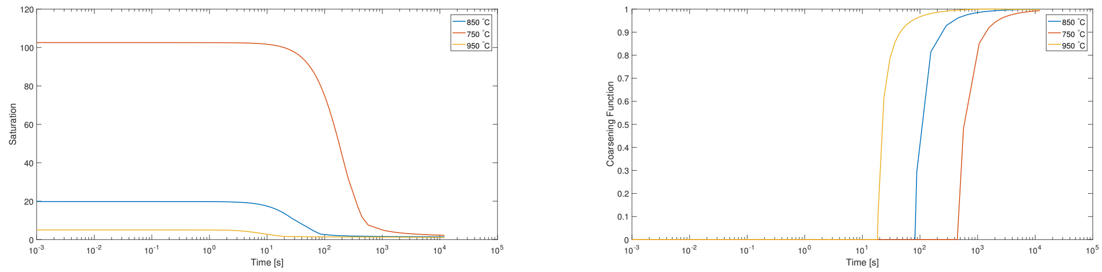

(c) Saturation.

(d) Coarsening function.

Figure 6.16: Simulation results for different temperatures and $\rho = 3.27 \times 10^{14}\ \mathrm{m}^{-2}$.

Non-isothermal calculations

During hot rolling, the material is being heated and non-isothermal reactions take place. To model this process, we implement a temperature curve depending on time. Using the restrictions on the temperature given at the beginning of this section, we choose the following two temperature schemes for our non-isothermal simulations.

(a) Linear temperature increase from 850 °C to 1000 °C in 140 minutes, after which the temperature stays constant, to simulate the hot rolling process.

(b) Non-linear temperature increase from 728.36 °C to 1000 °C based on experimental temperature data.

The implemented temperature curves are given in Figure 6.17.

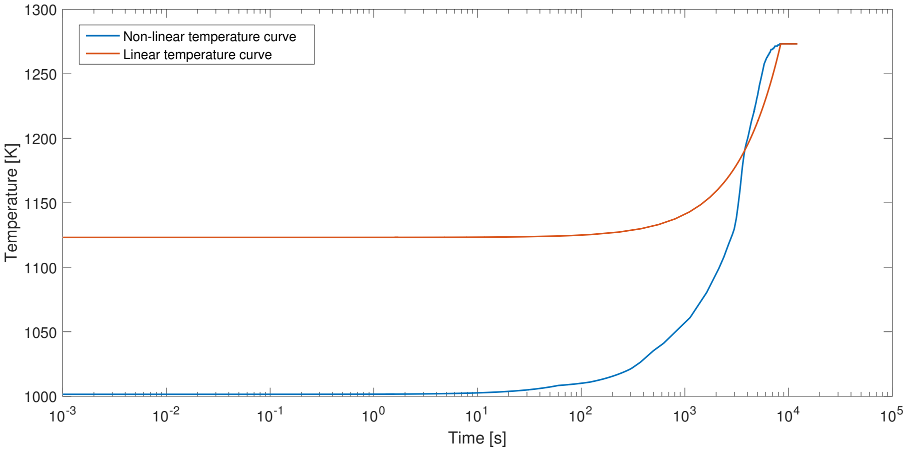

Figure 6.17: Linear (setting (a)) and non-linear (setting (b)) temperature curves in time.

The temperature curves have different starting temperatures, but reach the same final temperature, slightly below the solvus temperature. The results of the non-isothermal calculation with the linear temperature increase (setting (a)) are shown in Figure 6.18 and the results of the non-isothermal calculation with the non-linear temperature increase (setting (b)) are shown in Figure 6.20.

For the linear temperature increase (Figure 6.18), the development of both the precipitate radius and precipitate number density follow the results for 850 °C, because the temperature also starts at 850 °C. Eventually the density drops faster and the diameter grows faster then the 850 °C-results, more agreeing with the 950 °C-results, because of the temperature increase to 1000 °C. This could mean that results for non-isotherm calculations could constructed using parts of the isotherm calculations. However, more simulations with special temperature curves (for example high temperature peaks) should be run to test this presumption. In Figure 6.18d the coarsening function drops below one at some point. When we plot both the volume fraction and the equilibrium volume fraction corrected for the Gibbs-Thomson effect (Figure 6.19), we can see this is because at high temperatures the volume fraction increases above the equilibrium volume fraction and precipitates start to dissolve, i.e. the coarsening function drops below one. The behavior of the saturation in time is not changed by the temperature increase and is only influenced by the starting temperature, as shown in Figure 6.18c.

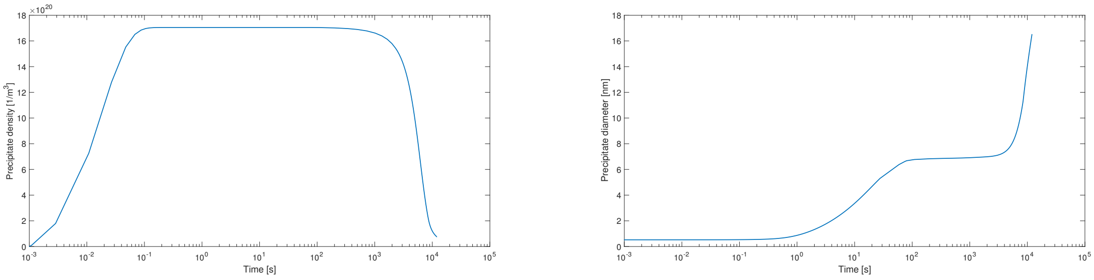

(a) Precipitate number density.

(b) Precipitate diameter.

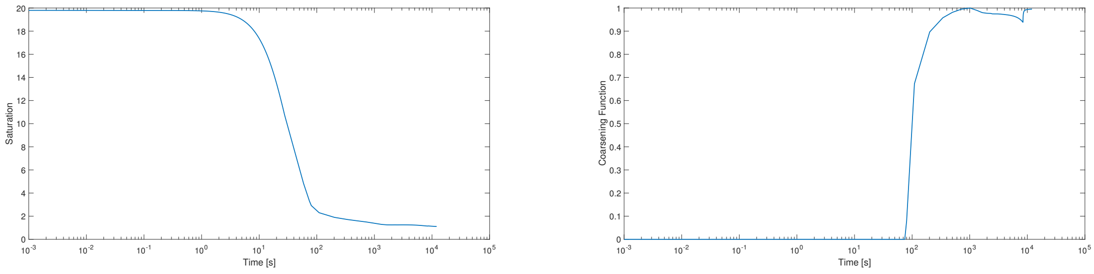

(c) Saturation.

(d) Coarsening function.

Figure 6.18: Simulation results for a linear temperature increase and $\rho = 3.27 \times 10^{14}$ m^{-2}.

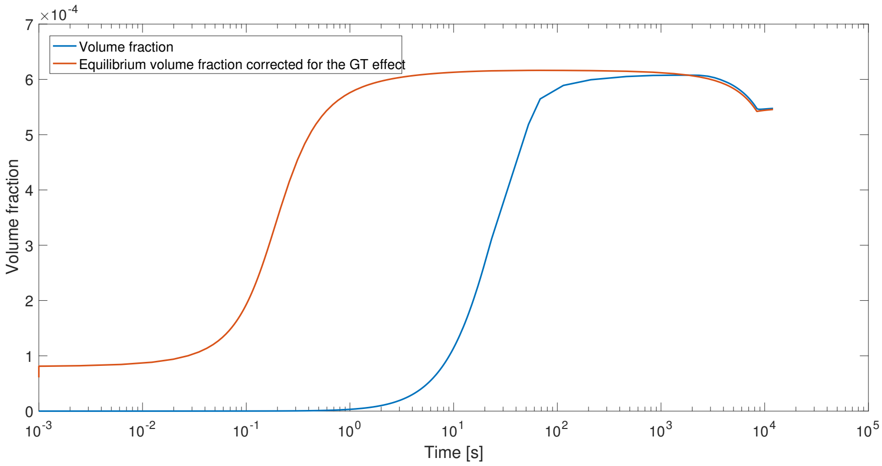

Figure 6.19: Volume fraction and equilibrium volume fraction corrected for the Gibbs-Thomson effect in time with a linear temperature increase and $\rho = 3.27 \times 10^{14}$ m^{-2}.

When using the non-linear temperature increase (setting (b)), we get the results shown in Figure 6.20. The temperature curve is based on experimental temperature data. Unfortunately the experimental temperature data took values above our solvus temperature, so we equally decreased the temperature to below the solvus temperature, resulting in the temperature curve in Figure 6.17. The results in Figure 6.20 look similar to those found for the linear temperature increase, except for the more oscillating coarsening function and the much higher saturation. In the plot for the volume fraction in Figure 6.21 we see that the volume fraction gets slightly above the equilibrium volume fraction, as with the linear temperature increase, and therefore the coarsening function drops below one. The precipitate mean diameter even decreases when the coarsening starts, due to the large decrease in the coarsening function right after it reached one. The coarsening function recovers to one and the precipitate mean diameter start growing again. The oscillations in the coarsening function can not be physically explained and are probably due to numerical errors or the definition of the coarsening function. Since the volume fraction does not have the oscillations, regularisation of the coarsening function by Perrard et al. (2007) could solve the problem. The high saturation agrees with earlier results: lower temperatures mean a higher saturation, and the behavior is not influenced by the temperature curve.

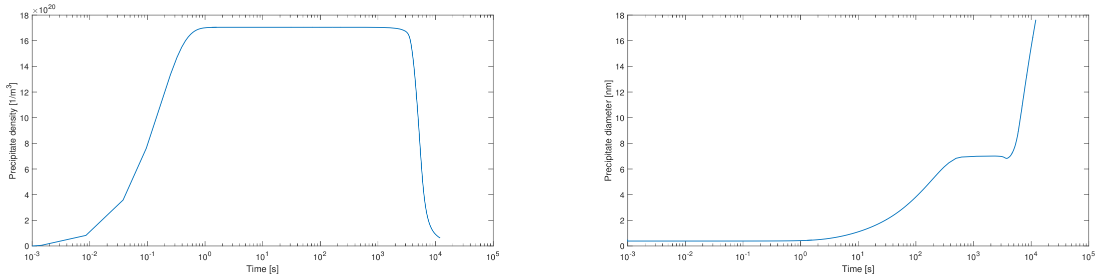

(a) Precipitate number density.

(b) Precipitate diameter.

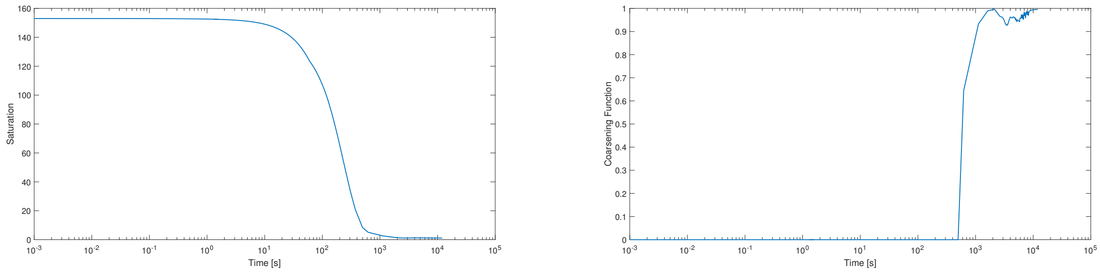

(c) Saturation.

(d) Coarsening function.

Figure 6.20: Simulation results for a non-linear temperature increase and $\rho = 3.27 \times 10^{14}$ m^{-2}.

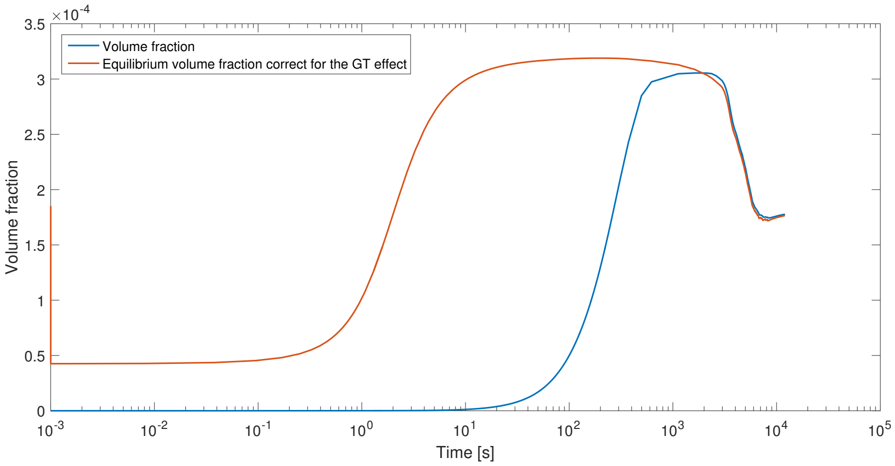

Figure 6.21: Volume fraction and equilibrium volume fraction corrected for the Gibbs-Thomson effect in time with a non-linear temperature increase and $\rho = 3.27 \times 10^{14}$ m^{-2}.

6.3.3. Dislocation density

In the simulations, discussed in the previous sections, the dislocation density was taken to be equal to 3.27×10^{14} m^{-2}. However from Kranendonk (2005) we find, when taking the evolution of the dislocations into account by involving recovery and recrystallisation models in the simulation, the initial dislocation density can be reduced by a factor two in the time interval of 12000 seconds. Therefore we test our model for different dislocation densities:

(a) 3.27×10^{14} m^{-2}, the original dislocation density from previous simulations,

(b) 1.18×10^{14} m^{-2}, about half the original dislocation density,

(c) 6.54×10^{14} m^{-2}, about double the original dislocation density.

The dislocation density ρ occurs twice in the precipitation model.

1. In the maximum number of potential nucleation sites N_{total}, which is defined by (Equation (3.1))

$$N_{total} = \frac{F\rho}{b}.$$

2. In the effective diffusion coefficient D_{eff}, which is defined by (Equation (3.10))

$$D_{eff} = D_{pipe}\pi b^2 \rho + D_{bulk}(1 - \pi b^2 \rho).$$

We expect that when we decrease the dislocation density, the plateau in the precipitate density will also decrease, but the mean diameter will increase and vice versa. So positive effects on the density plateau and opposite effects on the mean diameter. This because the maximum volume fraction (Equation (6.1)) stays the same, independent of the dislocation density. The influence from the effective diffusion coefficient on the results is probably low. The results of the simulations are given in Figure 6.22.

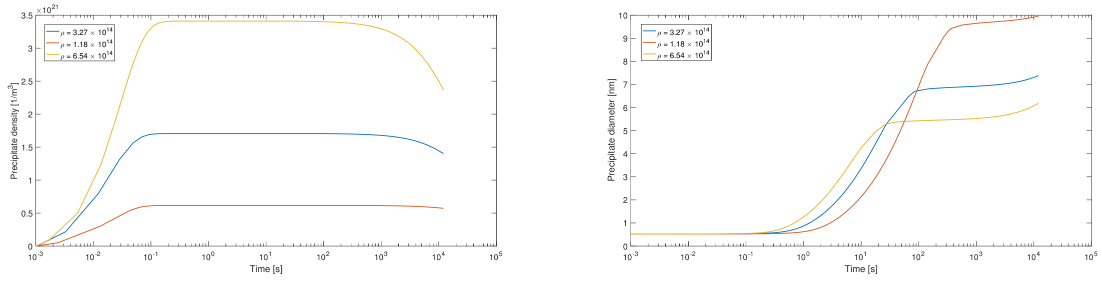

(a) Precipitate number density.

(b) Precipitate mean diameter.

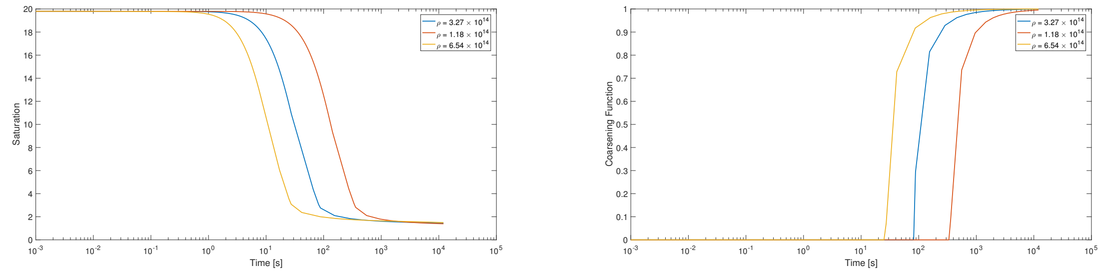

(c) Saturation.

(d) Coarsening function.

Figure 6.22: Simulation results for different dislocation densities at 850 °C.

When we look at the results of the simulation using different dislocation densities, it confirms our expectations on the effect of the dislocation density. However, the precipitate mean diameter shows an interesting inversion phenomenon. Increasing the dislocation density increases the growth rate, but the plateau in the precipitate growth is also reached sooner, furthermore the plateau is at a lower value. This is attributed to the lower number of nucleation sites and since the final volume fraction is the same, the average particle radius

should be larger. Growth curves for lower dislocation densities start later but continue for a longer period and therefore cross the growth curves belonging to higher dislocation densities.
Also, the results show that increasing the dislocation density expedites the coarsening (Figure 6.22d) and the decrease of the saturation (Figure 6.22c).

6.3.4. Chemical composition

In this section, the influence of the composition will be studied, by comparing the results of composition N1, presented in the previous sections, with the alloys N2 and N4 presented in Table 6.8. The results of the simulation are given in Figure 6.23.

Table 6.8: Alloy composition of alloys N1, N2 and N4 used in the simulations in weight percentages (Kranendonk (2005)).

Alloy	C	Si	Mn	P	S	Nb	Al	N	Fe
N1	0.076	0.06	1.34	0.0058	0.0026	0.03	0	0.0061	93.3815
N2	0.20	0.20	1.0	0.024	0.013	0.007	0.006	0.0056	98.5444
N4	0.21	0.19	1.14	0.023	0.015	0.058	0.008	0.0061	98.3499

Since we are only focusing on NbC_xN_{1-x} precipitates, we expect that just the weight percentages of Nb, C and N will have influence on the results. When we compare the weight percentages of these elements in the three different alloys we find the following table.

Table 6.9: Initial weight percentages and fractions of the precipitate elements together with the solvus temperatures.

Alloy	Nb	C	N	X_{Nb}	X_C	X_N	T_{sol} (°C)
N1	0.03	0.076	0.0061	1.7947×10^{-4}	0.0035	2.4201×10^{-4}	1093.88
N2	0.007	0.20	0.0056	4.1628×10^{-5}	0.0092	2.2085×10^{-4}	1021.21
N4	0.058	0.21	0.0061	3.4488×10^{-4}	0.0097	2.4054×10^{-4}	1240.30

When comparing the different weight fractions of Nb, C and N in the different alloys, we find that Nb determines the maximum volume fraction in alloys N1 and N2 since it has the lowest weight fraction. A higher concentration of the element determining the maximum volume fraction, leads to a higher maximum volume fraction. To remind, the volume fraction is defined by (Equation (6.1))

$$f_v = \frac{4}{3}\pi N R^3,$$

meaning that a higher maximum volume fraction thereby leads to larger precipitates (R), since the maximum number of precipitates (N) will not be influenced (if the dislocation density is the same for all three compositions).

Figure 6.23 confirms our expectations for alloys N1 and N2. It shows that the mean diameter of N1 is larger than the mean diameter of N2 and the same effect can be seen in the saturation, which is defined by (Equation (3.5))

$$\text{saturation} = \frac{\text{matrix product}}{\text{solubility product}}.$$

However, the higher saturation is mainly due to the initial matrix product which is different for each chemical composition. For N4 a volume fraction based analysis cannot be made this easily, since Nb is not the determining element for the volume fraction, but nitrogen (N) is. Nevertheless, the results show that the higher weight percentage of Nb in N4 compared to the other two alloys still results in larger precipitates. For the duration of precipitation, we find that the starting point of nucleation of N2 is later then that of N1 and N4, and ends earlier. Even though, the decrease in nucleation for N4 is the latest, the start of nucleation is second. We can conclude that when Nb determines the maximum volume fraction, a higher maximum volume fraction will lead to later nucleation. When Nb does not determine the maximum volume fraction, no clear conclusion can be stated from these results.

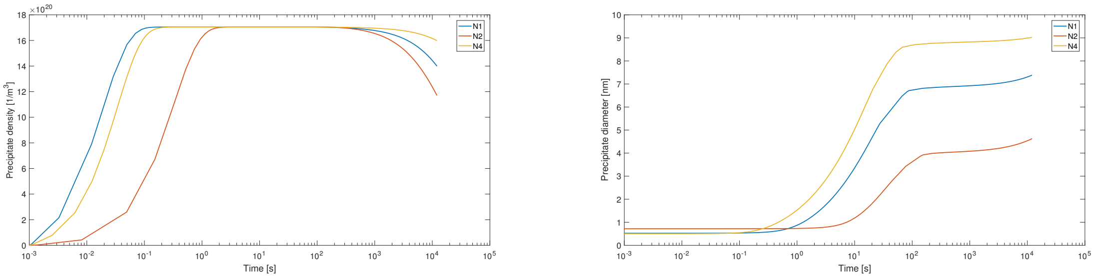

(a) Precipitate number density.

(b) Precipitate mean diameter.

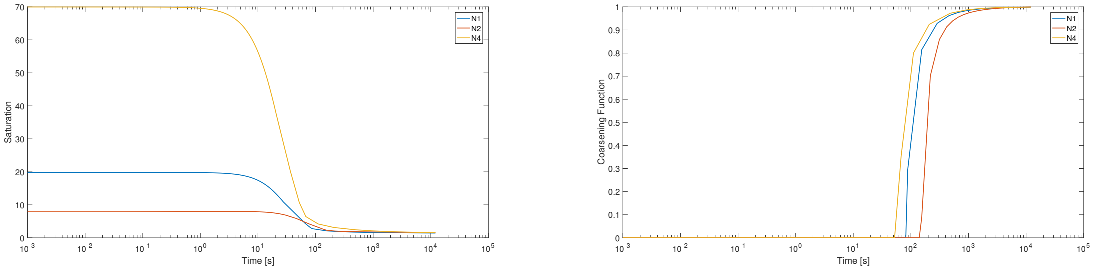

(c) Saturation.

(d) Coarsening function.

Figure 6.23: Simulation results for different chemical compositions at 850 °C and $\rho = 3.27 \times 10^{14}$.

7

Concluding remarks and future work

In this literature study, the precipitation model by Zurob et al. (2002) has been implemented, analysed and improved. For the solving of the differential equations different numerical methods have been tested and the results compared to the results found by Kranendonk (2005). During the implementation some computational issues arose because of the model, but after some adjustments in the implementation these issues were solved.

Various initial values and parameters have been varied to see the effect on the results and the performance of the implementation. All results of the simulations could be qualitatively interpreted. Also, the model is quite robust, but the computation time can increase drastically when different initial constants are chosen (like a high temperature or high starting density). This is mainly because of the non-linear equations in the model, like the critical radius and the interface concentration, that have be solved in every time step during the simulation.

Even though the results we find using the precipitation model by Zurob et al. (2002) seem to be realistic and predict the experimental data quite well after fitting, for applications to modern steel grades the Zurob models needs a number of improvements and extensions:

- The approximation for $Z\beta^*$ in the nucleation rate during the first stage could be improved, but also the approximation for N_{total} in this equation, which involves an adjustable factor F which has no direct physical meaning. From data fitting we even find a value for F about three orders of magnitude lower than expected.

- Because most steel alloys frequently contain many alloying elements, different precipitates can occur simultaneously (for instance, Nb(C,N), AlN, MnS) and complex precipitates may exist, like (Nb, Ti)(C,N). In the Zurob model, only one type of precipitate is considered at the time. For future work it would be nice to be able to also describe the nucleation and growth of multiple types of precipitates at the same time, since this is more realistic. A multi-component model is the extension to capture this complexity (Den Ouden (2015)).

- A serious disadvantage of the Zurob model is the use of the mean radius of the precipitates. The difference between small and large precipitates or only average sized precipitates can not be found in this way. An improvement for this would be to use distributions for the size of the precipitates, in which you can see how many precipitates of that specific size exist. For homogeneous nucleation such an implementation is already done by Den Ouden (2015), but for heterogeneous nucleation this still has to be developed. After which the two models for homogeneous and heterogeneous nucleation could be combined. An additional advantage of the distribution implementation is that it is not necessary to distinguish a nucleation and growth stage from a coarsening stage, because both stages are covered in the evolution of the precipitate size distribution.

Once the improvements on the precipitation model are completed, this model has to be linked to the original recrystallisation and recovery models by Zurob et al. (2002). And if time allows it, also improvements in these models could be made.

Taking these considerations into account, the steps that need to be performed:

1. Make a new model with distributions, based on the old model.
2. Improve the new model with a multi-component version.
3. Improve the physical approximations made in the Zurob model, of which some are described previously (like the approximation for $Z\beta^*$).
4. Couple the new model to the recrystallisation and recovery models.
5. Improve the recrystallisation and recovery model.
6. Add the homogeneous precipitation model to the system.

A

The recrystallization model and recovery model as developed by Zurob et al.

- Recrystallisation

$$
\begin{aligned}
X(t) &= 1 - \exp\left(-N_{rex}\left(\int_0^t M(t)G(t)\,dt\right)^3\right) \\
N_{rex} &= \frac{kS_v}{A_c} \\
M(t) &= \left(\frac{1}{M_{pure}} + \alpha C_{NB}^M\right)^{-1} \\
G(t) &= \frac{1}{2}\rho(t)\mu b^2 - \frac{3\gamma_{gb}F_v(t)}{R(t)}
\end{aligned}
$$

- Recovery

$$
\begin{aligned}
\frac{d\sigma_p}{dt} &= -\frac{64\sigma_p^2 v_d}{9M^3\alpha_r^2 E}\exp\left(-\frac{U_a}{k_B T}\right)\sinh\left(\frac{\sigma_p V_a}{k_b T}\right)\left(1-\frac{N}{N_c}\right), \text{For } N < N_c \\
\frac{d\sigma_p}{dt} &= 0, \text{For } N > N_c \text{where } U_a = 286\ \text{kJ/mole}\ , V_a = 45b^3, N_c = \frac{1}{2}\rho(t)^{1.5}, \sigma_p = \sigma - \sigma_y
\end{aligned}
$$

B

Dimensional analysis of the differential equation for the precipitate number density N in the Zurob model

The differential equation for the precipitate number density N is given by

$$\frac{dN}{dt} = (N_{total} - N)\left(\frac{D_{pipe}\mathbf{C}}{a^2}\right)\exp\left(\frac{-\Delta G^*}{k_b T}\right)$$

with dimensions

$$\begin{aligned}\frac{1}{[\mathrm{m}^3]}\frac{1}{[\mathrm{s}]} &= \left(\frac{1}{[\mathrm{m}^3]} - \frac{1}{[\mathrm{m}^3]}\right)\left(\frac{\frac{[\mathrm{m}^2]}{[\mathrm{s}]}[?]}{[\mathrm{m}^2]}\right)\exp\left(\frac{[\mathrm{J}]}{\frac{[\mathrm{J}]}{[\mathrm{K}]}[\mathrm{K}]}\right),\\ \frac{1}{[\mathrm{m}^3]}\frac{1}{[\mathrm{s}]} &= 1\frac{1}{[\mathrm{m}^3]}\frac{[?]}{[\mathrm{s}]}1.\end{aligned}$$

So $\mathbf{C}$ should be dimensionless, and therefore equals the molar fraction x_{Nb}^{M} and not the concentration C_{Nb}^{M} (Zurob et al. (2002)).

C

Conversion formulas as used in the simulations

In the implementation of the models, we use a set of conversion formulas from Kranendonk (2005). The symbols used in these formulas are:

Table C.1: Used symbols in the conversion formulas

Symbol	Property	Unit
C_X^M	Concentration of element X in the matrix	$\mathrm{mol/m^3}$
M_j	Molar weight of component j	kg/mol
wt_j	Weight fraction of component j [1]	
x_j	Molar fraction of component j	
ρ_{aus}	Mass density of austenite	$\mathrm{g/m^3}$

[1] Note that in the implementation the weight percentage is used, where $wt_j = \frac{wt\%j}{100}$.

The formulas are given by (for a system with N components)

$$x_j = \frac{\frac{wt_j}{M_j}}{\sum\limits_{k=1}^{N} \frac{wt_k}{M_k}},$$

$$wt_j = \frac{x_j M_j}{\sum\limits_{k=1}^{N} x_k M_k},$$

and

$$wt_X = \frac{C_X^M M_X}{\rho_{aus}},$$

$$C_X^M = \frac{wt_x \rho_{aus}}{M_X}.$$

D

Standard settings as used in the simulation

Solubility products

$$K(NbC) = 10^{3.42-\frac{7900}{T}}$$
$$K(NbN) = 10^{2.80-\frac{8500}{T}}$$

Mass densities

$$\rho_{NbCN} = \frac{M_{Nb} + xM_C + (1-x)M_N}{v_{m,NbCN}} \quad \text{g/m}^3$$
$$\rho_{aus} = (8283.8 - 0.5785 \cdot T) \cdot 1000 \quad \text{g/m}^3$$

Lattice constant

$$a = (0.36306 + 0.078x_c)(1 + (24.9 - 50x_c)(T - 1000) \times 10^{-6}) \times 10^{-9} \quad \text{m}$$

Molar volumes

$$v_{m,NbCN} = xv_{m,NbC} + (1-x)v_{m,NbN} \quad \text{m}^3\text{/mol}$$
$$v_{m,aus} = \frac{1}{4}N_a a^3 \quad \text{m}^3\text{/mol}$$

Interface energy

$$\gamma = 2.5 \times 10^{-5}(T_{sol} - T)^{1.5} + 0.375 \quad \text{J/m}^2$$

Shear modulus

$$\mu = 81 \times 10^9 \left(1 - 0.91\frac{T - 300}{1810}\right) \quad \text{Pa}$$

Diffusion coefficients

$$D_{pipe} = 4.1 \times 10^{-4} \exp\left(\frac{-172500}{R_g T}\right) \quad \text{m}^2\text{/sec}$$
$$D_{bulk} = 0.83 \times 10^{-4} \exp\left(\frac{-266500}{R_g T}\right) \quad \text{m}^2\text{/sec}$$

Coarsening Function

$$F_c = 1 - \text{erf}\left(4\left(\frac{R}{R_0}\ln\left(\frac{C^M_{Nb}}{C^{Eq}_{Nb}}\right) - 1\right)\right) \quad \text{(with restrictions from Kranendonk (2005))}$$

Differential equations and functions

$$\begin{aligned}
\frac{dN}{dt} &= (1 - F_c)\frac{dN}{dt}\bigg|_{\text{nucleation}} + F_c \frac{dN}{dt}\bigg|_{\text{coarse}}, \\
\frac{dR}{dt} &= (1 - F_c)\frac{dR}{dt}\bigg|_{\text{nucleation,growth}} + F_c \frac{dR}{dt}\bigg|_{\text{coarse}},
\end{aligned}$$

where

$$\begin{aligned}
\frac{dN}{dt}\bigg|_{\text{nucleation}} &= (N_{total} - N)\left(\frac{D_{pipe} x^M_{Nb}}{a^2}\right)\exp\left(\frac{-\Delta G^*}{k_b T}\right), \\
\frac{dN}{dt}\bigg|_{\text{coarse}} &= \frac{4}{27}\frac{C^{Eq}_{Nb}}{C^P_{Nb} - C^{Eq}_{Nb}}\frac{R_0 D}{R^3}\left(\frac{R_0 C^M_{Nb}}{R(C^P_{Nb} - C^M_{Nb})}\left(\frac{3}{4\pi R^3} - N\right) - 3N\right), \\
\frac{dR}{dt}\bigg|_{\text{nucleation,growth}} &= \frac{D_{eff}}{R}\frac{C^M_{Nb} - C^R_{Nb}}{C^P_{Nb} - C^R_{Nb}} + \frac{1}{N}\frac{dN}{dt}(\alpha_n R^* - R), \\
\frac{dR}{dt}\bigg|_{\text{coarse}} &= \frac{4}{27}\frac{C^{Eq}_{Nb}}{C^P_{Nb} - C^{Eq}_{Nb}}\frac{R_0 D}{R^2}.
\end{aligned}$$

Bibliography

Academic Resource Center. Materials Deformation, 2015. URL https://web.iit.edu/sites/web/files/departments/academic-affairs/Academic%20Resource%20Center/pdfs/Material_Deformations_Workshop.pdf. Presentation, Last accessed 4 February 2016.

E. Alberdi Celaya, J.J. Anza Aquirrezabala, and P. Chatzipantelidis. Implementation of an Adaptive BDF2 Formula and Comparison with the MATLAB Ode15s. *Procedia Computer Science*, 29:1014–1026, 2014.

Cdan. Images - Material Science, own work, 2015. URL https://commons.wikimedia.org/wiki/User:Cdang/Gallerie_d%27images/Materials_sciences?uselang=nl. Last accessed 4 February 2016.

D. Den Ouden. *Mathematical Modelling of Nucleating and Growing Precipitates*. PhD thesis, Delft University of Technology, 2015.

A. Deschamps and Y. Brechet. Influence of predeformation and ageing of an Al-Zn-Mg alloy - II. Modeling of precipitation kinetics and yield stress. *Acta Materialia*, 47:293–305, 1999. Pergamon.

R.C. Hudd, A. Jones, and M.N. Kale. A method for calculating the solubility and composition of carbonitride precipitates in steel with particular reference to niobium carbonitride. *Journal of The Iron and Steel Institute*, pages 121–125, February 1971.

D. Hull and D.J. Bacon. *Introduction to Dislocations*. Butterworth-Heinemann, Linacre House, Jordan Hill, Oxford OX2 8DP, England, 2001.

W. Kranendonk. Modelling Strain Induced Precipitation: the Zurob Model, 2005. Tata Steel R&D, Reference Source number: 114496.

H. Kreye. Einfluß von Versetzungen auf die Umlösing von Teilchen. *Zeitschrift für Metallkunde*, 61:108–112, 1970.

Learning Geology. Elementary concepts of thermodynamics, 2015. URL http://geologylearn.blogspot.nl/2015/11/elementary-concepts-of-thermodynamics.html. Last accessed 4 February 2016.

Mathworks. Ode15s, 2016. URL http://nl.mathworks.com/help/matlab/ref/ode15s.html. Last accessed 22 February 2016.

Jitin Nair. What is an intuitive explanation of the iron-carbon phase diagram?, 2015. URL https://www.quora.com/What-is-an-intuitive-explanation-of-the-iron-carbon-phase-diagram. Last accessed 4 February 2016.

M. Perez, M. Dumont, and D. Acevedo-Reyes. Implementation of classical nucleation and growth theories for precipitation. *Acta Materialia*, 56:2119–2132, 2008.

F. Perrard, A. Deschamps, and P. Maugis. Modelling the precipitation of NbC on dislocations in α-Fe. *Acta Materialia*, 55:1255–1266, 2007.

D.A. Porter and K.E. Easterling. *Phase Transformations in Metals and Alloys*. Chapman & Hall, 2-6 Boundary Row, London SE1 8HN, England, 1981.

M. Rendy Yusman. Hot Working of Metals, 2011. URL http://sainsmechanical.blogspot.nl/2011/12/hot-working-of-metals.html. Last accessed 2 March 2016.

P. Rey. P. Rey's Teaching Portofolio, 2015. URL http://www.geosci.usyd.edu.au/users/prey/Teaching/Teach.html. Last accessed 4 February 2016.

K.P. Shah. The Hand Book on Mechanical Maintenance - Crystallization, 2012. URL http://practicalmaintenance.net/. Last accessed 4 February 2016.

C. Vuik, F. Vermolen, M.B. Van Gijzen, and M.J. Vuik. *Numerical methods for ordinary differential equations.* VSSD, Leeghwaterstraat 42, 2628 CA Delft, The Netherlands, 2015.

Wikipedia. Steelmaking, 2015. URL https://en.wikipedia.org/wiki/Steelmaking. Last accessed 17 December 2015.

Wikipedia. Backward differentiation formula, 2016a. URL https://en.wikipedia.org/wiki/Backward_differentiation_formula. Last accessed 22 February 2016.

Wikipedia. Burgers vector, 2016b. URL https://en.wikipedia.org/wiki/Burgers_vector. Last accessed 4 February 2016.

Wikipedia. Allotropes of iron, 2016c. URL https://en.wikipedia.org/wiki/Allotropes_of_iron. Last accessed 4 February 2016.

Wikipedia. Numerical methods for ordinary differential equations, 2016d. URL https://en.wikipedia.org/wiki/Numerical_methods_for_ordinary_differential_equations. Last accessed 16 March 2016.

Wikipedia. Basic oxygen steelmaking, 2016e. URL https://en.wikipedia.org/wiki/Basic_oxygen_steelmaking. Last accessed 4 February 2016.

H.S. Zurob. *Effects op precipitation, recovery and recrystallization on the microstructural evolution of microalloyed austenite.* PhD thesis, McMaster University, 2003.

H.S. Zurob, C.R. Hutchinson, Y. Brechet, and G. Purdy. Modeling recrystallization of microalloyed austenite: effect of coupling recovery, precipitation and recrystallization. *Acta Materialia*, 50:3075–3092, 2002. Pergamon.

Nomenclature

Numerical symbols

α	Parameter used in the adaptive time step algorithm	
β	Parameter used in the adaptive time step algorithm	
h	Time step	s
h_{start}	Initial time step	
N_{max}	Maximum number of iterations for Picard's method	
t_{end}	End time	
t_{start}	Starting time	
TOL	Tolerance level for the Picard iteration	

Precipitation related symbols

α_n	Numerical factor, accounting for the fact that nucleated precipitates can grow only if their radius is slightly larger than the nucleation radius	
ΔG^*	Activation energy for the nucleation of a precipitate (on a dislocation)	J
ΔG_d	Free energy release due to the reduction of the elastic energy of a dislocation	J
Δg_v	Driving force for precipitation	J/m^3
γ	Interfacial energy between precipitate and matrix	J/m^2
μ	Shear modulus of steel	Pa
ν	Poisson ratio	
ρ	Dislocation density	$1/m^2$
ρ_{aus}	Mass density of austenite	g/m^3
a	Lattice constant of austenite	m
b	Burgers vector	m
C_X^0	Initial concentration of element X in the matrix	mol/m^3
C_X^P	Concentration of element X in precipitates	mol/m^3
C_X^R	Equilibrium concentration of element X with average radius R	mol/m^3
C_X^M	Concentration of element X in the matrix	mol/m^3
C_X^{Eq}	Equilibrium concentration of element X in the matrix at infinite time	mol/m^3
D_{bulk}	Diffusion coefficient in the bulk	m^2/s
D_{eff}	Effective diffusion coefficient	m^2/s
D_{pipe}	Diffusion coefficient in the pipe	m^2/s
F	Adjustable factor smaller than 1	

F_c	Coarsening function	
f_v	Volume fraction	
$f_{v,GT}$	Equilibrium volume fraction, corrected for the Gibbs-Thomson effect	
f_v^{Eq}	Equilibrium volume fraction	
f_v^{Init}	Initial volume fraction	
$K(NbC)$	Solubility product of niobium carbide	
$K(NbC_xN_{1-x})$	Solubility product of niobium carbonitride	
$K(NbN)$	Solubility product of niobium nitride	
k_b	Boltzmann constant	J/K
M_X	Molar weight of element X	g/mol
$N(t)$	Number density of precipitates as a function of time	$1/\mathrm{m}^3$
N_a	Number of Avogadro	1/mol
N_{total}	Maximum number density of precipitation per nucleation site	$1/\mathrm{m}^3$
$R(t)$	Mean radius of precipitates over time	m
R^*	Critical precipitate nucleus radius for heterogeneous nucleation at a dislocation	m
R_h^*	Critical precipitate nucleus radius for homogeneous nucleation	m
R_g	Gas constant	J/(K mol)
T	Temperature	K
t	Time	s
T_{sol}	Solvus temperature	K
$v_{m,aus}$	Molar volume of austenite	$\mathrm{m}^3/\mathrm{mol}$
$v_{m,NbCN}$	Molar volume of $\mathrm{Nb(C}_x\mathrm{N}_{1-x})$	$\mathrm{m}^3/\mathrm{mol}$
$v_{m,NbC}$	Molar volume of NbC	$\mathrm{m}^3/\mathrm{mol}$
$v_{m,NbN}$	Molar volume of NbN	$\mathrm{m}^3/\mathrm{mol}$
v_{NbCN}	Volume per atom $\mathrm{Nb(C}_x\mathrm{N}_{1-x})$	m^3
$wt\%X^0$	Initial weight percentage of element X	
$wt\%X^M$	Weight percentage of element X in the matrix	
$wt\%X^P$	Weight percentage of element X in the precipitate	
$wt\%X^{Eq}$	Equilibrium weight percentage of element X in the matrix at infinite time	
$wt\%X^{R27/23}$	Equilibrium weight percentage of element X with average radius $\frac{27}{23}R$	
$wt\%X^R$	Equilibrium weight percentage of element X with average radius R	
wt_X^i	Weight fraction of elements X with special condition i, like Eq, R, etc. (as with the weight percentages)	
x	Stoichiometric ratio of carbon and nitrogen in the precipitate niobiumcarbonitride ($\mathrm{NbC}_x\mathrm{N}_{1-x}$) at equilibrium	
x_X^M	Molar fraction of X in the matrix	